Energy & Environmental Science

Cite this: *Energy Environ. Sci.*, 2011, **4**, 4380

www.rsc.org/ees

PERSPECTIVE

From Ni-YSZ to sulfur-tolerant anode materials for SOFCs: electrochemical behavior, *in situ* characterization, modeling, and future perspectives

Zhe Cheng,†[a] Jeng-Han Wang,[b] YongMan Choi,‡[a] Lei Yang,[a] M. C. Lin[cd] and Meilin Liu*[ae]

Received 17th May 2011, Accepted 8th July 2011
DOI: 10.1039/c1ee01758f

Solid oxide fuel cells (SOFCs) offer great promise for the most efficient and cost-effective conversion to electricity of a wide variety of fuels such as hydrocarbons, coal gas, and gasified carbonaceous solids. However, the conventional Ni-YSZ (yttria-stabilized zirconia) anode is highly susceptible to deactivation (poisoning) by contaminants commonly encountered in readily available fuels, especially sulfur-containing compounds. Thus, one of the critical challenges facing the realization of fuel-flexible and cost-effective SOFC systems is the development of sulfur-tolerant anode materials. This *perspective* article aims at providing a comprehensive review of materials that have been studied as anodes for SOFCs, the electrochemical behavior of various anode materials in H_2S-contaminated fuels, experimental methods for *ex situ* and *in situ* characterizations of species and phases formed on anode surfaces upon exposure to H_2S-containing fuels, mechanisms for the interactions between H_2S and anode surfaces as predicted from density functional theory (DFT) calculations, and possible strategies of minimizing or eliminating the effect of sulfur poisoning. While significant progress has been made in developing alternative anode materials with better sulfur tolerance, in probing and mapping electrode surface species relevant to sulfur poisoning, and in unraveling the mechanisms of H_2S–anode interactions using both computational and experimental approaches, many challenges still remain to bridge the gaps between models at different scales or between theoretical predictions and experimental observations. An important new direction for future research is to develop a predictive multi-scale (from DFT to continuum) computational framework, through a rigorous validation at each scale by carefully-designed experiments performed under *in situ* conditions, for rational design of better sulfur-tolerant anode materials and structures for a new generation of SOFCs to be powered by readily available fuels.

[a]*Center for Innovative Fuel Cell and Battery Technologies, School of Materials Science and Engineering, Georgia Institute of Technology, Atlanta, Georgia, 30332, USA. E-mail: meilin.liu@mse.gatech.edu; Tel: +1-404-894-6114*
[b]*Department of Chemistry, National Taiwan Normal University, Taipei, 11677, Taiwan, ROC*
[c]*Department of Chemistry, Emory University, 1515 Dickey Drive, Atlanta, Georgia, 30322, USA*
[d]*Center for Interdisciplinary Molecular Science, National Chiao Tung University, Hsinchu, 30010, Taiwan, ROC*
[e]*World Class University (WCU), UNIST, South Korea*
† Current address: Central Research & Development, E. I. du Pont de Nemours & Company, Wilmington, Delaware 19880, USA.
‡ Current address: Chemistry Department, Brookhaven National Laboratory, Upton, New York 11973, USA.

Broader context

Solid oxide fuel cells (SOFCs) offer great prospects for the most efficient utilization of a wide variety of chemical fuels, from hydrocarbon fuels to carbonaceous solid fuels (such as coal, biomass, and municipal solid waste). For example, combined-heat-and-power systems based on SOFCs are twice as efficient as today's coal-fired power plants, potentially reducing CO_2 emission by 50%. Before SOFCs can be widely adopted, however, several hurdles must be overcome: high cost, poor durability, and anode deactivation or degradation by contaminants, especially sulfur in a variety of readily available fuels. Even renewable hydrocarbon sources like biogas also contain sulfur contaminants. Thus, the development of sulfur-tolerant anode materials and structures represents a grand challenge facing the commercialization of economically competitive SOFCs. To date, extensive efforts have been devoted to gaining a profound understanding of the sulfur–anode interactions using both experimental and theoretical approaches and have led to discoveries of some promising alternative anode materials that display superior sulfur tolerance while maintaining high performance and ease of fabrication. These findings would not only advance the SOFC technology but also benefit research in other related areas like desulfurization catalysts for fuel processing and materials for corrosion inhibition in sulfur-containing environments.

1 Introduction

The demand for clean, secure, and sustainable energy sources has stimulated great interests in fuel cells, electrochemical devices that directly convert the energy of a chemical fuel to electricity. Among all types of fuel cells, solid oxide fuel cells (SOFCs) offer great prospects for the most efficient utilization of various readily available carbon-containing fuels[1–5] such as natural gas,[6–9] gasified coal,[10–14] and other solid carbonaceous fuels including municipal solid waste and biomass.[15–17] For example, simulations have shown that SOFC systems run on natural gas or gasified coal can be much more efficient than today's combustion-based power generation systems, considerably reducing CO_2 emission.[5,18–24]

Schematically shown in Fig. 1 is a single SOFC based on a solid oxide electrolyte that conducts oxygen ions and/or protons. The three key components of each individual cell include a gas impermeable layer of ceramic electrolyte, a porous anode where the fuel is electrochemically oxidized, and a porous cathode where the oxidant (usually oxygen from the air) is electrochemically reduced. The state-of-the-art SOFCs are based on yttria-stabilized zirconia (YSZ) electrolyte and Ni-YSZ cermet anodes. The prevailing cathodes for commercial use are strontium-doped lanthanum manganese oxide

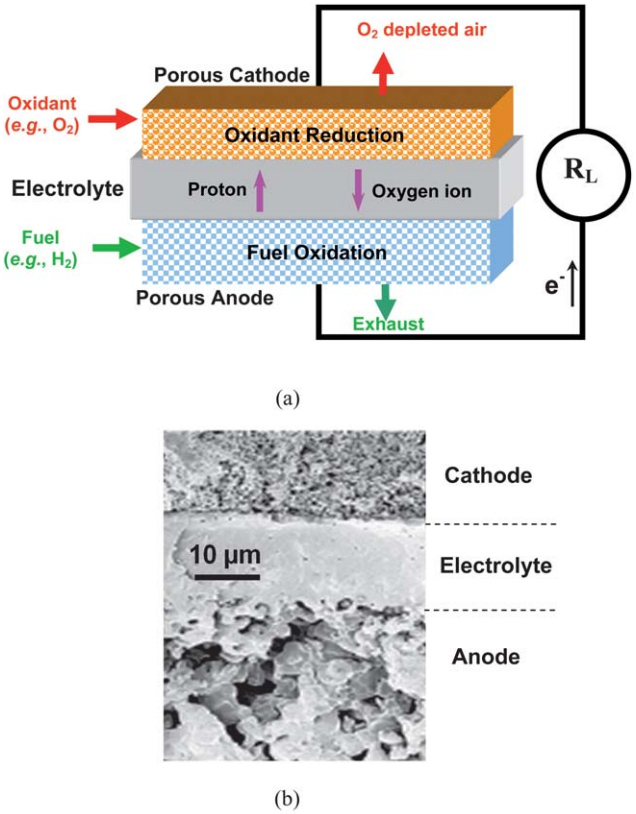

Fig. 1 (a) A schematic for an SOFC single cell and (b) a cross-sectional view (SEM micrograph) of a single cell with a thin (~12 μm) electrolyte.

Zhe Cheng

Zhe Cheng is a research scientist at the Central Research & Development Division of E. I. du Pont de Nemours and Company in Wilmington, Delaware, USA. He received his BS from Tsinghua University in Beijing, China, and both MS and PhD from Georgia Institute of Technology in Atlanta, Georgia, USA. Zhe's PhD advisor was Professor Meilin Liu, and his thesis focused on studying sulfur-anode interaction mechanisms and developing novel sulfur-tolerant anode materials for solid oxide fuel cells. His current research is on advanced electrode materials for lithium ion batteries and new metallization and passivation materials for silicon solar cells.

Jeng-Han Wang

Jeng-Han Wang obtained his PhD in Chemistry from Emory University, Atlanta, Georgia, USA. He then worked as a postdoctoral fellow in the School of Materials Science and Engineering at Georgia Institute of Technology, Atlanta, Georgia, USA. In 2008, he accepted an Assistant Professor position in the Chemistry Department at National Taiwan Normal University, Taipei, Taiwan. His research interests include the investigation of mechanisms for gas-surface interfacial reactions and understanding the fundamental chemistry of heterogeneous catalysts for the better design of novel materials. His current research activities focus on the reforming of carbon-containing feedstocks for hydrogen production.

Meilin Liu

Meilin Liu is a Regents' Professor of Materials Science and Engineering and Co-Director of the Center for Innovative Fuel Cell and Battery Technologies at Georgia Institute of Technology, Atlanta, Georgia, USA. He received his BS from South China University of Technology and MS and PhD from University of California at Berkeley. His research interests include in situ characterization and multi-scale modeling of charge and mass transfer along surfaces, across interfaces, and in membranes, thin films, and nanostructured electrodes, aiming at achieving rational design of materials and structures with unique functionalities for efficient energy storage and conversion.

($La_{1-x}Sr_xMnO_{3-\delta}$, LSM) or strontium-doped lanthanum cobalt-iron oxide ($La_{1-x}Sr_xCo_yFe_{1-y}O_{3-\delta}$, LSCF).

However, one crucial problem associated with using hydrocarbon fuels in SOFCs is that most of those fuels contain sulfur compounds to some extent, which are converted to gaseous hydrogen sulfide (H_2S) upon reforming,[8,17,25] and the current Ni-YSZ anodes for SOFCs as well as the reforming catalysts (if an external reforming is performed) are readily deactivated or poisoned by such sulfur contaminants. As a result, a desulfurization unit is usually added in typical SOFC systems before the reformer or the anode (in the case of internal reforming),[5] as schematically shown in Fig. 2, which adds complexity and cost and decreases system efficiency. Furthermore, in the effort to lower the operating temperature (to 750 °C and below)[26] so that cheaper metallic materials could be used for interconnection, researchers have found that the critical sulfur concentration at which sulfur poisoning becomes significant also *decreases* precipitously as the cell operating temperature is reduced (*e.g.*, ~0.05 parts-per-million, ppm, at 750 °C),[27] making sulfur removal extremely demanding and sulfur poisoning a problem of even greater importance and urgency.

In the past few decades, extensive efforts have been devoted to characterizing sulfur poisoning behavior of conventional Ni-YSZ cermet anodes, unraveling the mechanism of sulfur poisoning, and developing alternative anode materials with enhanced sulfur tolerance. This *perspective* article aims to provide a comprehensive review of the current understanding of sulfur–anode interactions under typical SOFC operating conditions. In *Section 2*, we start with a brief discussion of the general requirements for SOFC anode materials, the characteristics of the conventional Ni-YSZ cermet anodes, and the sulfur poisoning behavior of Ni-YSZ anodes. In *Section 3*, we then present the behavior of various alternative anode materials that have been explored for sulfur tolerance. In *Section 4*, we focus on *in situ* and *ex situ* characterizations of the interactions between anode materials and H_2S as well as some new insights into the interpretation of the results. In *Section 5*, we summarize the current status in calculations based on density functional theory (DFT) for prediction of energetics, reaction sequence, and intermediates of the interactions between H_2S and anode/electrolyte, Further, *ab initio* atomistic thermodynamics calculations are applied to rationalize the conditions that favor sulfur poisoning and/or regeneration and to identify the bulk and surface phases resulted from the poisoning process. These fundamental understandings are vital to revealing the atomistic mechanism for sulfur–anode interactions and have provided us with useful insights into the design of new sulfur-tolerant anode materials. In *Section 6*, we focus on a new approach to achieving sulfur tolerance using $Ba(Ce_{1-x}Zr_x)O_3$-based materials as the electrolyte phase in the cermet anode while keeping Ni as the primary electronic conductor and electro-catalyst. The hypotheses regarding sulfur removal reactions for such anodes are also provided. Finally, we provide in *Section 7* some concluding remarks and future perspectives in the design of better anode materials for a new generation of SOFCs to be powered by readily available and renewable fuels.

2 Electrochemical behavior of the Ni-YSZ anode in sulfur-containing fuels

2.1. General requirements for SOFC anodes and properties of Ni-YSZ cermet anode

As discussed earlier in various review articles,[28–34] the general requirements for SOFC anode materials include high electronic conductivity, excellent catalytic activity towards electro-oxidation of fuels, sufficient ionic conductivity to extend the active sites beyond the anode–electrolyte interfaces, suitable porosity to allow the fuel molecules to flow towards and reaction products away from the active sites, adequate durability and compatibility with other SOFC components during cell fabrication and operation, robust mechanical and thermal stability, easy fabrication, and low cost. In addition, other desirable (but may not yet be fully achieved) properties[35] include tolerances to carbon deposition,[36] sulfur poisoning,[33,35] and re-oxidation.[37]

For SOFCs based on the YSZ electrolyte, porous metal-ceramic composites or cermets, especially Ni-YSZ cermets, are the most widely used anodes among many materials explored. The electrical conductivities of nickel metal, YSZ (in particular, 8 mol% yttria stabilized zirconia or 8YSZ), and a typical Ni-YSZ cermet (with a volume ratio of 8YSZ to Ni of 40 : 60 and a porosity of 30%) at elevated temperatures (*e.g.*, 700–1000 °C) are on the order of $\sim 10^4$ S cm^{-1}, 10^{-2} to 10^{-1} S cm^{-1}, and $\sim 10^2$ to 10^3 S cm^{-1}, respectively.[35] In cell fabrication, the precursor of nickel, nickel oxide (NiO), is often co-fired with the YSZ electrolyte. The relatively low solubility of NiO in YSZ (~2 to 5%)[38] allows co-firing of the NiO-YSZ anode supported thin YSZ electrolyte at high temperatures (~1450 °C). The catalytic activity of the Ni-YSZ anode toward oxidation of clean H_2 is excellent, and at temperatures < ~800 °C, anode polarization resistance decreases dramatically with increasing current density.[39] YSZ, NiO, and Ni have *average* coefficients of thermal

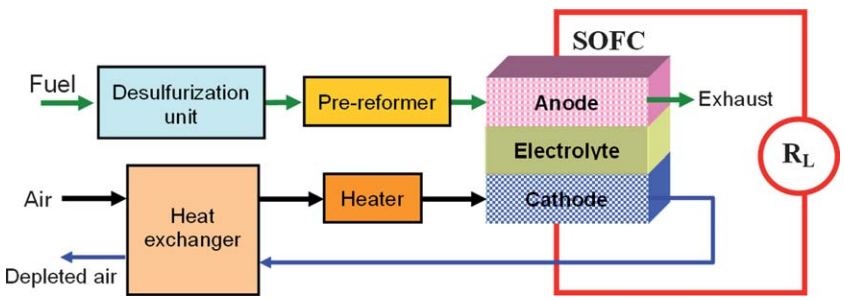

Fig. 2 A simplified schematic for an SOFC system.

expansion (CTE) of ~11.0 × 10^{-6} K^{-1}, ~14.0 × 10^{-6} K^{-1}, and ~14.6 × 10^{-6} K^{-1}, respectively, and a typical Ni-YSZ cermet anode has an *average* CTE of ~12.5 × 10^{-6} K^{-1}, which is a reasonable match with that for the 8YSZ electrolyte.[40–42] (Note *average* CTE is used because the CTE for these materials usually varies slightly with temperature in the range of ~20 to 1000 °C.) The mechanical strength of Ni-YSZ cermet is on the order of 100 MPa,[28,43] which is about one half of that for dense YSZ.[44] It is a reasonable value considering that the Ni-YSZ cermet anode in the reduced state usually has a porosity of ~30% and a Ni to YSZ volume ratio from approximately 30 : 70 to 60 : 40.[35] While the coarsening of Ni grains and associated performance degradation have been reported in the literature,[32,45] commercial SOFC stacks based on Ni-YSZ cermet anodes, especially those with tubular structures, have successfully demonstrated stable operation for tens of thousands of hours with very little degradation at temperatures as high as 900–1000 °C,[18,46–49] indicating that the stability for the Ni-YSZ cermet anode is *adequate* under SOFC operating conditions when the composition and microstructures are optimized.

2.2. Sulfur poisoning behavior of Ni-YSZ cermet anodes

Schematically illustrated in Fig. 3 is a typical experimental arrangement for electrochemical measurements of an electrolyte-supported SOFC button cell, which is commonly used for detailed investigation into the sulfur poisoning behavior of anode materials under different conditions. With properly positioned reference electrodes, the anodic polarization resistance and the degree of anode poisoning (or the *increase* in anode polarization resistance due to sulfur poisoning) can be determined from 3 (or 4)-electrode measurements using different electrochemical techniques like impedance spectroscopy. Alternative cell designs for proper positioning of reference electrodes are available elsewhere.[50,51]

Schematically shown in Fig. 4 are different sulfur poisoning behaviors observed for SOFCs with Ni-YSZ anodes upon exposure to hydrogen contaminated with low concentration (ppm level) H_2S. In all cases, there is a rapid initial drop in power output upon exposure to ppm-level H_2S, which is associated with a large and rapid increase in anode polarization resistance and has been the focus of most studies in the literature.[27,35,52–61] In this section, we will provide a review of the sulfur poisoning behavior of conventional Ni-YSZ anodes with a focus on clarifying the effects of various factors on the observed *initial rapid sulfur poisoning*, including operating conditions (*e.g.*, temperature and gas concentration), cell structures, and materials used. The mechanism for the initial rapid degradation due to sulfur poisoning will also be discussed based on observed electrochemical behavior and theoretical modeling. In addition, different behaviors have been observed for Ni-YSZ anodes after exposure to a sulfur-containing fuel for a *long* period of time, as schematically shown in Fig. 4. The behavior during long-term exposure, together with the regeneration process for Ni-YSZ anodes, will also be discussed at the end of this section.

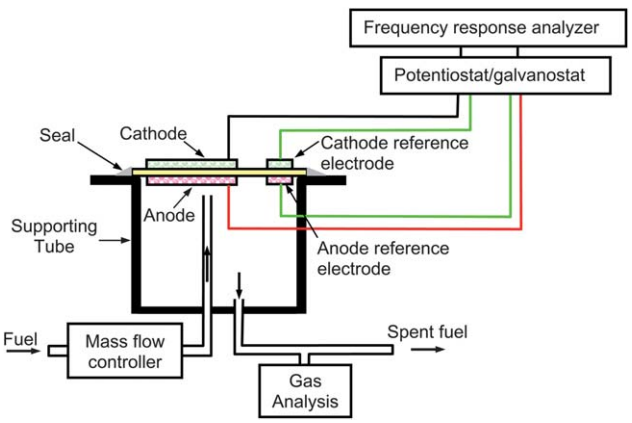

Fig. 3 Schematic for the electrochemical measurement system for an SOFC button cell with reference electrodes on both anode and cathode sides.

2.2.1. Effects of operating temperature

•*Normal operating temperatures (>~650 °C).* Operating temperature significantly influences the observed sulfur poisoning behavior of a Ni-YSZ anode. Typically, the observed relative drop in power output due to sulfur poisoning, $\Delta P_r = (P - P^S)/P$ (in which P and P^S are power output before and after initial quick sulfur poisoning, respectively), *increases with decreasing temperature* (except when the cells operated at a temperature ≤~650 °C as to be discussed later). For example, Singhal *et al.* observed that at a current density of 160 mA cm^{-2}, 2 ppm H_2S in the fuel led to a drop in cell voltage by 2% and 9% at 1000 °C and 900 °C, respectively.[52] This is corroborated later by Matsuzaki and Yasuda's study on the anode interfacial resistance: under open circuit conditions, the anodic interfacial resistance increased by 18% and 72% at 1000 °C and 900 °C, respectively, upon exposure to 2 ppm H_2S, while at 750 °C, 0.7 ppm H_2S resulted in an increase in anode interfacial resistance by as much as 105%.[27] Presented in Fig. 5 are the effects of temperature as well as pH_2S/pH_2 on the relative power output drop ΔP_r due to sulfur poisoning for SOFC button cells reported by Zha *et al.*[54]

•*Complications at very low temperatures.* As the cell operating temperature is reduced to ~650 °C *or lower*, the observed apparent trend in relative power output drop due to sulfur poisoning ΔP_r could change. For example, Zha *et al.* found that ΔP_r actually became smaller with decreasing temperature for an electrolyte-supported button cell in a fuel with $pH_2S/pH_2 = 1$ ppm: 12% at 700 °C, 8% at 650 °C, and 6% at 600 °C.[62] This appears opposite to the trend observed at 700 °C and above, as shown in Fig. 5: 4% at 900 °C, 8% at 800 °C, and 12% at 700 °C. Unfortunately, no additional information regarding anode/electrolyte interfacial impedance or polarization was available to pinpoint the exact cause of these trends.

The change in observed poisoning behavior with temperature at ~650 °C and below is due most likely to the change in relative contribution of the anode to the total resistance of the cell. At higher temperatures, the relative increase in anode polarization resistance due to sulfur poisoning $\Delta R^S_{pa\_r} = (R^S_{pa} - R_{pa})/R_{pa}$ (in which R_{pa} and R^S_{pa} are anode polarization resistances before and after initial quick sulfur poisoning, respectively) has a greater impact on the total cell resistance[51] and, thus, on the observed ΔP_r. In contrast, at lower temperatures (*e.g.*, ~650 °C and

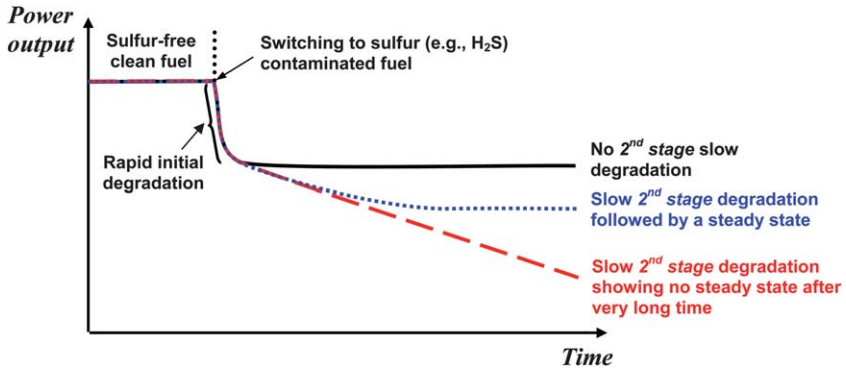

Fig. 4 Schematic for power output *versus* time for SOFCs with Ni-YSZ cermet anode showing sulfur poisoning with rapid initial degradation followed by different *2nd stage* behaviors: (solid line) no *2nd stage slow degradation*: power output saturates right after initial rapid degradation; (dotted line) a slow *2nd stage* degradation followed by a steady state; (dashed line) a slow *2nd stage* degradation showing no steady state after very long time (*e.g.*, thousands of hours).

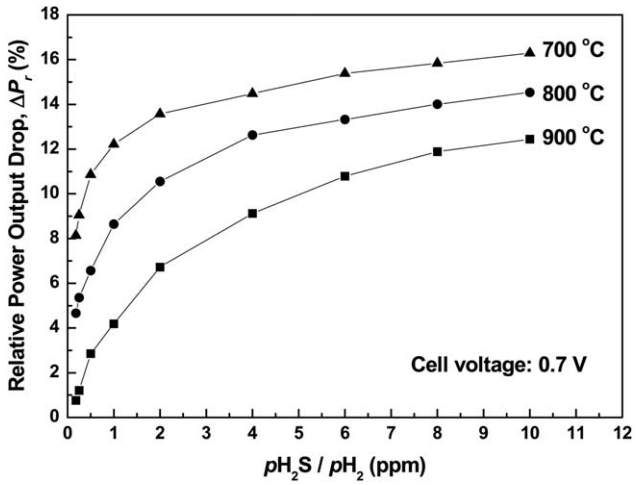

Fig. 5 Relative power output drop due to sulfur poisoning, ΔP_r, *versus* pH_2S/pH_2 at different temperatures for the electrolyte-supported SOFC button cell operated at a constant voltage of 0.7 V. Adopted from Zha *et al.*[54] with modifications.

below), although $\Delta R^S_{pa\_r}$ might be larger due to (slightly) higher sulfur coverage on nickel,[63–66] (see Section 5) the *relative* impact of anode sulfur poisoning on total cell resistance becomes less significant as cathode polarization contributes more to the total cell resistance,[51,67] leading to the observed decrease in ΔP_r.

2.2.2. Effects of H_2S, H_2, H_2O, CO, and CO_2 concentrations

•*H_2S.* Since the equilibrium coverage of adsorbed sulfur on the nickel surface increases with the H_2S concentration in the fuel at a given temperature,[63–66] (see Section 5.2.1) the relative *change* in anode polarization resistance due to sulfur poisoning $\Delta R^S_{pa\_r}$ increases with H_2S concentration. Fig. 6 shows the data reported by Matsuzaki: at 900 °C, $\Delta R^S_{pa\_r}$ increased first rapidly and then gradually as the pH_2S/pH_2 increased from 0.5 ppm to 8 ppm.[27] Similar behavior was also observed in the relative drop in power output ΔP_r, as seen in Fig. 5.

A striking feature with H_2S poisoning is the sensitivity of the Ni-YSZ anode towards the minuscule (*sub ppm-level*) concentration of H_2S at intermediate to low temperatures. For example, Matsuzaki and Yasuda found that, at 750 °C, the polarization resistance for the Ni-YSZ cermet anode increased by ~28% when the pH_2S/pH_2 was only 0.05 ppm, as shown in Fig. 6.[27] Such high sensitivity at intermediate temperatures had also been observed by others under similar conditions. For example, at 750 °C with only 0.1 ppm H_2S, Waldbillig *et al.* reported that the cell voltage dropped ~10% at a constant current density of 500 mA cm^{-2},[61] while Sprenkle *et al.* reported that the cell current density dropped by ~30% at a constant voltage of 0.7 V.[57,68]

It should be noted that the apparent influence of H_2S concentration on sulfur poisoning depends also on temperature. For example, at 900 °C, changing the sulfur concentration from 0.5 to 8 ppm led to an increase of $\Delta R^S_{pa\_r}$ from 37% to 108%, as seen in Fig. 6.[27] In contrast, our study shows that at 600 °C the change in ΔP_r or total cell interfacial resistance was almost negligible when the pH_2S/pH_2 increased from 1 to 10 ppm.[62] As discussed earlier in Section 2.2.1, such behavior is related to the *relative* contribution of the anode to the total resistance of the cell at different temperatures. It is also related to the intrinsic

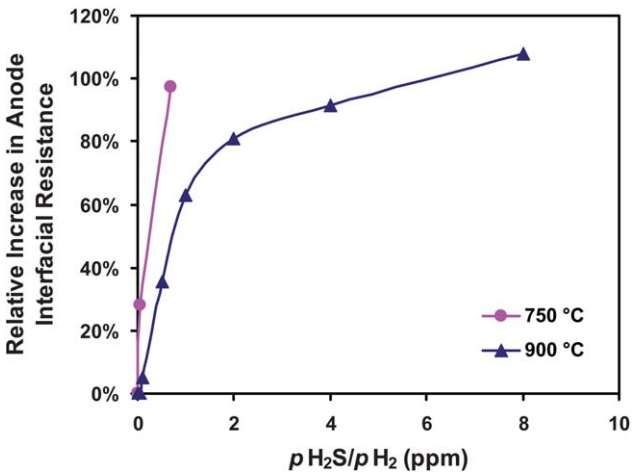

Fig. 6 Relative increase in anode interfacial resistance, $\Delta R^S_{pa\_r}$, *versus* pH_2S/pH_2 for Ni-YSZ cermet anodes at 750 and 900 °C. Data from Matsuzaki and Yasuda.[27]

adsorption behavior of sulfur on nickel, as to be discussed later in Section 5.2.1.

•*H_2 and H_2O.* The effect of H_2 concentration on sulfur poisoning behavior is *not* pronounced under typical operating conditions. For example, Li *et al.* found that increasing the H_2 concentration from 27% to 53% has *no* observable effect on the sulfur poisoning behavior.[69] On the other hand, at a low temperature of 600 °C, Lohsoontorn *et al.* observed that cells with the Ni-gadolinia doped ceria (GDC) anode underwent an obvious increase in anodic interfacial resistance when the H_2 concentration was decreased from 97% to 9.7% and the poisoning became less reversible.[70]

Similarly, the effect of water vapor concentration on sulfur poisoning appears insignificant under typical operating conditions.[54] On the other hand, Li *et al.* found that using a fuel with very high H_2S concentration (pH_2S/pH_2 of 0.2% or 2000 ppm), higher water vapor concentration in the fuel seems to slow down the poisoning process and reduce the observed relative drop in power output due to sulfur poisoning (ΔP_r): at 800 °C under a constant current density of 0.5 A cm^{-2}, the cell voltage drop was 180 mV, 161 mV, and 108 mV when the fuel water vapor content was 0%, 3%, and 10%, respectively.[71] It is also noted that in an experiment using Ni-YSZ as the catalyst for reforming (not under SOFC conditions), the presence of H_2O in the fuel stream leads to enhanced SO_2 desorption.[72]

•*CO and CO_2.* CO may exert dramatic influence on the extent of sulfur poisoning only when the molar ratio of H_2 to CO is very low.[11,53,69,73] For example, Sasaki *et al.* found that for fuel mixtures of H_2 and CO, the effect of CO concentration on ΔP_r was relatively small until the H_2 to CO ratio was 1 to 9 or lower and the shift reaction became ineffective due to sulfur poisoning, thus limiting the hydrogen supply.[53] In addition, Li *et al.* found that the effect of CO was more significant in the regeneration process: cell performance recovered much slower in a H_2–CO fuel mixture than in hydrogen upon removal of H_2S.[69]

In contrast, CO_2 concentration has no observable effect on sulfur poisoning. For example, the behavior of a Ni-YSZ anode running in a spent fuel consisting of 85% CO_2, 10% CO, and 5% H_2 at 1000 °C upon exposure to 50 ppm H_2S[73] appears similar to that observed in CO_2-free fuels.

•*Hydrocarbons.* According to the study by Rasmussen and Hagen, in the presence of low concentration of light hydrocarbons like methane, the sulfur poisoning behavior for the Ni-YSZ anode is *not* significantly influenced, but the internal reforming activity is dramatically reduced.[74] High concentration of hydrocarbon or heavy hydrocarbons (*e.g.*, butane, octane, diesel, or kerosene) would make the reaction process much more complicated due to the complex natures of reforming and other associated reactions like thermal cracking and carbon deposition, and they are beyond the scope of this paper.

To summarize, of common gas species in the fuel, the H_2S concentration, in particular pH_2S/pH_2, has the greatest impact on the observed sulfur poisoning behavior, while the concentration of other gaseous species only matters under certain, sometimes extreme, conditions.

2.2.3. Effects of anodic polarization (current density or voltage)

•*Observed effects on ΔP_r and ΔR_{cell_r} and related hypothesis.* As to the influence of anodic polarization or current density/voltage on the observed sulfur poisoning behavior, the following are some common observations. First, the relationship between observed relative drop in cell power output due to sulfur poisoning ΔP_r and cell current density/voltage depends on the operating conditions: under constant voltage (potentiostatic) conditions, ΔP_r tends to *decrease* with increasing polarization (*i.e.*, higher current density),[54,55,57] while under constant current (galvanostatic) conditions, ΔP_r tends to *increase* with increasing polarization (*i.e.*, higher current density).[52,55,57,61] The different trends in ΔP_r with respect to anodic polarization observed under constant voltage *versus* constant current conditions have been explained by Cheng *et al.* using circuit analysis[55] and by Sprenkle *et al. via* comparing the changes in *I–V* curves before and after sulfur poisoning.[57] Second, the observed relative increase in total cell resistance due to sulfur poisoning, $\Delta R_{cell\_r} = (R^S_{cell} - R_{cell})/R_{cell}$ (in which R_{cell} and R^S_{cell} are the total cell resistance before and after sulfur poisoning, respectively), tends to *decrease* with increasing polarization (*i.e.*, higher cell current density or lower cell terminal voltage) no matter whether the measurement is carried out under constant voltage or constant current conditions.[55]

The above observation leads to the hypothesis that larger oxygen ion flux induced by higher current density may lead to increased electrochemical oxidation of sulfur species on the anode *via* the following reaction[53–55]

$$S^* + 2O^{2-} = SO_{2(g)} + 4e^-, \quad (1)$$

or

$$S^* + 2O^x_o = SO_{2(g)} + 2V_{o^{\cdot\cdot}} + 4e^-. \quad (2)$$

where S* represents an adsorbed sulfur atom on the anode surface. The electrochemical oxidation of sulfur may diminish the degree of sulfur poisoning *via* reducing the sulfur surface coverage on the anode.

•*Other different observations on $\Delta R^S_{pa\_r}$.* However, it is noted that the observations made above are based on single cell tests using a two-electrode configuration so that the anodic interfacial resistance cannot be separated from the total cell resistance. For studies that actually separate anode polarization from cathode, the result seems to be quite different. For example, Primdahl and Mogensen found that at 1000 °C the relative increase in anode polarization resistance upon exposure to 35 ppm H_2S, $\Delta R^S_{pa\_r}$ did *not* change as the anodic current density was increased from zero (*i.e.*, open circuit conditions) to 100 mA cm^{-2}.[75] One possibility is that the higher anodic current density did not impact the extent of sulfur poisoning under the conditions they investigated. Another speculation is that there may be some decrease in the degree of sulfur poisoning due to surface sulfur removal by the oxygen ions, but that was countered by a small increase in mass transfer resistance under the testing conditions. More careful electrochemical measurements or direct chemical identification are required to fully understand the implications.

•*Non-linear behavior of interfacial polarization.* It is well known that the polarization resistance of an electrode depends on the current or overpotential (η) except in the linear region near equilibrium, where the polarization resistance approaches the "charge transfer resistance" defined as $j \rightarrow 0$ or $\eta \rightarrow 0$. Clearly when the cell current density (j) is sufficiently small, it is linearly related to the anode overpotential (η_a) as follows:[76]

$$\eta_a = jR_{pa} \tag{3}$$

where the anode polarization resistance (R_{pa}) is related to the anode exchange current density (j_0) and the anodic and cathodic transference numbers (α_a and α_c) by

$$R_{pa} = \frac{RT}{(\alpha_a + \alpha_c)Fj_0} \tag{4}$$

Then, the anode polarization resistance before poisoning R_{pa} and after sulfur poisoning R^S_{pa} should have the following relationship:

$$\frac{R^S_{pa}}{R_{pa}} = \frac{j_0}{j^S_0}, \tag{5}$$

if the anodic and cathodic transference numbers remain the same after sulfur poisoning. Under this assumption, the relative increase in anode polarization resistance due to sulfur poisoning, $\Delta R^S_{pa\_r}$, will be

$$\Delta R^S_{pa\_r} = \frac{R^S_{pa}}{R_{pa}} - 1 = \frac{j_0}{j^S_0} - 1 \tag{6}$$

Therefore, $\Delta R^S_{pa\_r}$ would be *independent of anode polarization (current density or anode overpotential)*.

Similarly, the observed difference in cell terminal voltage before sulfur poisoning, U, and after sulfur poisoning, U^S, at the same current density should depend linearly on current as follows:

$$\Delta U = U - U^S = \eta^S_a - \eta_a = jR^S_{pa} - jR_{pa} = j(R^S_{pa} - R_{pa}), \tag{7}$$

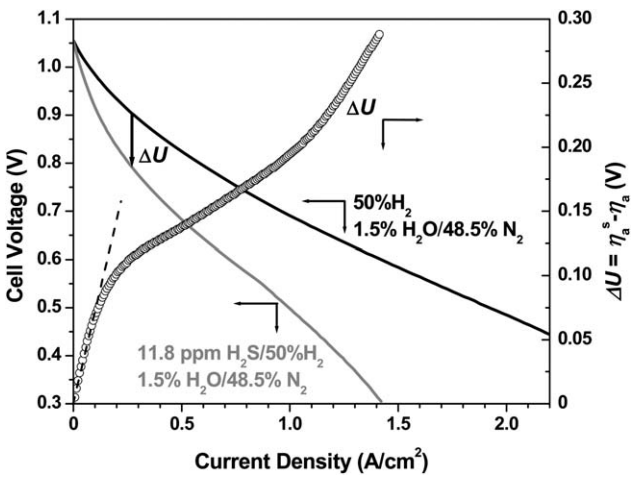

Fig. 7 Plots of cell voltage and the difference in anode overpotential $\Delta U = \eta^S_a - \eta_a$ *versus* cell current density for an anode-supported SOFC button cell before and after H_2S ($pH_2S/pH_2 = 11.8$ ppm) was introduced into the fuel stream of 50% H_2/1.5% H_2O/48.5% N_2 at 750 °C.

because the resistances of the cathode and the electrolyte are expected to remain constant. This has also been confirmed by experimental observation: Fig. 7 shows the current–voltage curves as well ΔU for cells before and after poisoning by H_2S ($pH_2S/pH_2 = 11.8$ ppm) at 750 °C for an anode-supported button cell, and ΔU has good linear dependence on the current density with a linear correlation coefficient better than 0.999 when $j <$ ~78 mA cm^{-2}.

In contrast, in the Tafel region (without mass transfer limitation), the relationship between the anode overpotential η_a and anodic current density j can be described as follows,

$$\eta_a = a \ln \frac{j}{j_0}, \tag{8}$$

where a is a constant that can be determined from experiments. Thus, the anode polarization resistance R_{pa} can be estimated as

$$R_{pa} = \frac{\eta_a}{j} = \frac{a(\ln j - \ln j_0)}{j}. \tag{9}$$

After sulfur poisoning, we have

$$\eta^S_a = a^S \ln \frac{j}{j^S_0}, \tag{10}$$

$$R^S_{pa} = \frac{\eta^S_a}{j} = \frac{a^S(\ln j - \ln j^S_0)}{j}. \tag{11}$$

Although a and a^S are unknown, the following relationship holds for the anode polarization resistance before and after sulfur poisoning at a given current density:

$$\frac{R^S_{pa}}{R_{pa}} = \frac{a^S}{a}\frac{(\ln j - \ln j^S_0)}{(\ln j - \ln j_0)} = \frac{a^S}{a}\left(1 + \frac{\ln j_0 - \ln j^S_0}{\ln j - \ln j_0}\right), \tag{12}$$

The relative change in anode polarization resistance is then given by,

$$\Delta R^S_{pa\_r} = \frac{R^S_{pa}}{R_{pa}} - 1 = \frac{a^S}{a}\left(1 + \frac{\ln j_0 - \ln j^S_0}{\ln j - \ln j_0}\right) - 1. \tag{13}$$

This expression implies that, *in the Tafel region*, $\Delta R^S_{pa\_r}$ *decreases with current density regardless of* the ratio of a^S to a because $j^S_0 < j_0 < j$. This is the nature of Tafel polarization; suggesting that a decrease in $\Delta R^S_{pa\_r}$ with increasing current density does not necessarily mean that it is due to reduced degree of sulfur poisoning *via* reduced sulfur coverage.

In conclusion, these electrochemical measurements alone may not be able to provide critical insights into the effect of cell operating conditions (current or voltage) on the degree of sulfur poisoning. More careful electrochemical measurements on well-designed test cells alongside with direct chemical identification of surface species are required to gain insight into the mechanism of sulfur poisoning processes.

For simple electrochemical measurements, the anode polarization resistance under open circuit conditions (as determined from impedance spectroscopy) or anode exchange current density is the most direct representation of the degree of sulfur poisoning. Marina *et al.* reported that exchange current densities for $Sr_xLa_{1-x}TiO_3$ (LST)-based anodes obtained from impedance analysis under close to equilibrium conditions do match those extrapolated from polarization curves in the Tafel regions for different concentrations of H_2S.[77]

Table 1 Summary of reported time (in hours) for the quick poisoning stage to finish for different SOFC button cells in different studies

			Time for quick poisoning to finish/hours		
			pH_2S/pH_2 (ppm)		
Cell structure	References	Conditions	0.1	1	10
Anode-supported cell	Cheng[62]	750 °C, 0.2 A cm^{-2}	—	40	3.5
	Waldbillig *et al.*[61]	750 °C, 0.5 A cm^{-2}	200	30	—
	Sprenkle *et al.*[57,68]	750 °C, 0.7 V	120	20	2
	Yang *et al.*[82]	750 °C, 0.4 A cm^{-2}		32	15
Electrolyte-supported cell	Zha	800 °C, 0.7 V	—	0.1	0.05

2.2.4. Effects of anode structure. The anode structure or the content of Ni in the Ni-YSZ cermet anode will also influence the time it takes for the cell to reach a steady state after exposure to H_2S. For example, for electrolyte-supported or cathode-supported cells with relatively thin anodes, the initial quick poisoning process completes in a relatively short period of time, sometimes just a few minutes.[53,54] In contrast, for anode-supported cells with relatively thick anodes, the initial quick poisoning process may last for hours or even days, depending on the H_2S concentration, the amount of available anode, and even the fuel flow rate and utilization. For example, in the study by Sprenkle *et al.* on anode-supported button cells as shown in Table 1, the time for the initial quick poisoning process to complete is 120 h, 20 h, and 2 h when the H_2S concentration was 0.1 ppm, 1 ppm, and 10 ppm, respectively.[57,61,68] Similar observation was also made by other researchers.[62] The reason is easy to understand: the adsorption of sulfur on Ni (see Section 5) will propagate from the outer layer to the inner active layer of anode. Therefore, for a cell with a thick anode (~500 μm) as in an anode-supported cell, it would take a longer time for all Ni surfaces to reach a steady state of sulfur coverage; in contrast, for a cell with a thin anode (~30 μm), it would take less time for the Ni surfaces to reach a similar level of sulfur coverage.

2.2.5. Effects of other cell components (*i.e.*, electrolyte and cathode). Although only the polarization resistance of the anode is influenced by sulfur in the fuel, the electrolyte and cathode will have an *indirect* impact on the observed relative changes in cell power output ΔP_r or in total cell resistance ΔR_{Cell_r} due to sulfur poisoning. For example, an anode-supported cell (with a thicker anode) shows a more severe drop in power output upon exposure to a sulfur-containing fuel than an electrolyte-supported cell (with a thinner anode). As the electrolyte or cathode resistances decrease (so that the total cell resistance is more dominated by the anode), ΔR_{Cell_r} would increase more due to the higher contribution of the anode polarization resistance, leading to larger ΔP_r. An example of this is shown in Table 2 for anode-supported cells with the same anode and electrolyte, but with different cathode materials. As the cathode material is changed from LSM-based material to LSCF-based material, both ΔP_r and ΔR_{Cell_r} usually increase due to the higher contribution of the anode to the total cell resistance as the LSCF cathode normally shows lower polarization resistance than LSM, especially under small bias conditions.

2.2.6. Mechanism of the initial quick sulfur poisoning. We would like to pause here and discuss briefly about the sulfur poisoning mechanism for the Ni-YSZ cermet anode based on results from *electrochemical measurements*. As stated, sulfur poisoning of the Ni-YSZ cermet anode is characterized by a rapid initial drop in power output upon exposure to sulfur-containing fuels. The subsequent slower degradation as observed in some studies is discussed in the next section. Thermodynamic analysis indicates that bulk sulfides (nickel sulfides in particular) would *not* form under the typical SOFC operating conditions when the H_2S concentration is in the low ppm range. For example, at 750 °C, nickel sulfides like Ni_3S_2 do not form until pH_2S/pH_2 is higher than ~3600 ppm, and the YSZ anode has been shown to be stable against H_2S for up to the percentage level.[78] In contrast, it is observed that the performance of a Ni-YSZ anode drops dramatically when the pH_2S/pH_2 is only 0.05 ppm at that temperature.[27] This indicates that the degradation in performance (*i.e.*, sulfur poisoning) in low concentrations of H_2S under typical SOFC operating conditions is due *not* to formation of nickel sulfides but to adsorption of sulfur on the anode surface. This is also consistent with the observation that the rapid initial drops in performance come to completion within just a few minutes for thin anodes (~30 μm).

Table 2 Comparison of relative cell power output drop ΔP_r and calculated relative cell internal resistance increase ΔR_{Cell_r} for anode-supported cells with different cathode materials upon exposure to different concentrations of H_2S

	Relative power output drop ΔP_r		Relative increase in total cell resistance ΔR_{Cell_r}	
Cathode material and cell current density	1 ppm	10 ppm	1 ppm	10 ppm
LSM, 200 mA cm^{-2}	—	10.6%	—	37%
LSCF, 200 mA cm^{-2}	7.9%	11.5%	60%	68%
LSM, 400 mA cm^{-2}	10%	14.2%	27%	36%
LSCF, 400 mA cm^{-2}	8.5%	13.0%	30%	54%

Various analysis approaches have been explored to fit the experimental data into existing adsorption models. For example, Marina *et al.* measured exchange current density from polarization curves before (j_0) and after sulfur poisoning j_0^S, and calculated the equilibrium surface coverage ratio of sulfur on anode θ_S assuming $\theta_S = 1 - j_0^S/j_0$.[77] However, the data fitting for the Ni-YSZ anode to the Langmuir isotherm is inconclusive due to limited amount of data.

On the other hand, Hansen and Rostrup-Nielsen used a Temkin-like isotherm for describing sulfur adsorption[59,60,64]

$$\frac{pH_2S}{pH_2} = \exp\left(\frac{\Delta H_0^0(1-\alpha\theta_S)}{RT} - \frac{\Delta S_0}{R}\right), \quad (14)$$

with a ΔH_0^0 of 289 kJ mol^{-1}, a ΔS^0 of -19 J mol^{-1} K^{-1}, and a α of 0.69. The equilibrium surface coverage could be calculated as

$$\theta_S = 1.45 - 9.53\times10^{-5}T + 4.17\times10^{-5}\ln\frac{pH_2S}{pH_2}. \quad (15)$$

Hansen fitted the relative drop in power output ΔP_r data by Zha *et al.* and Cheng *et al.* with respect to calculated sulfur surface coverage θ_S and obtained a linear relationship. The intercept for zero ΔP_r on the θ_S axis is ~0.55 to 0.60 instead of zero.[59]

Because ΔP_r is influenced by other factors such as electrolyte and cathode, an even more straightforward fitting is obtained by plotting the relative anode exchange current density j_0^S/j_0 *versus* sulfur surface coverage θ_S (calculated from the Temkin-like isotherm in eqn (15)), and the result is shown in Fig. 8 using data available in the literature. (Note j_0^S/j_0 is calculated from relative change in anode polarization resistance under open circuit conditions mentioned in ref. 27 and 54.) This time, the relative exchange current density j_0^S/j_0 decreases linearly from unity towards zero as the sulfur surface coverage θ_S increases from 0.5 towards 1. The deviation at high surface coverage may be attributed to the limitation of the Temkin model under that condition.[60] It is interesting to note that, according to the fitting, the exchange current density is not impacted until the sulfur surface coverage is higher than ~0.5.

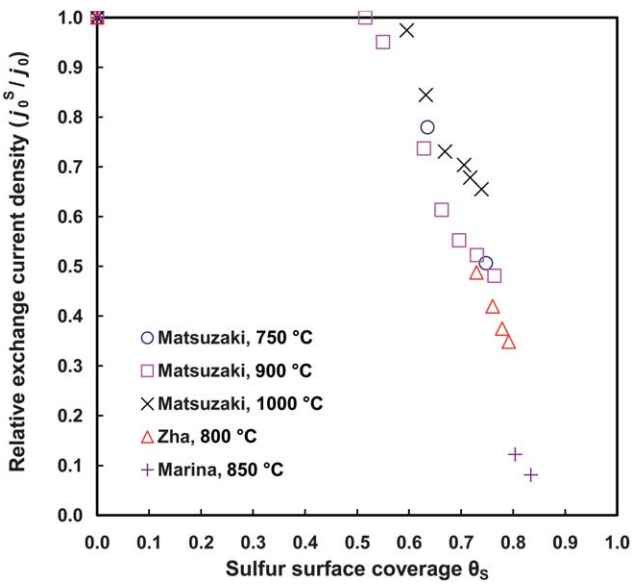

Fig. 8 Change of calculated relative exchange current density j_0^S/j_0 *versus* calculated sulfur surface coverage on Ni surface θ_S using data in the literature.[27,54,77]

2.2.7. Long-term sulfur poisoning behavior. Table 3 summarizes different long-term sulfur poisoning behaviors reported for SOFCs with the Ni-YSZ anode over extended periods of time (*i.e.*, hundreds of hours or even longer). As illustrated in Fig. 4, some studies show the cell power output reaches a steady state *right after* the initial quick poisoning stage. For example, in the study of Feduska and Isenberg, even though the initial pH_2S/pH_2 value was as high as 1000 ppm, no further performance degradation was observed in the next 800 h after the initial response reached a steady state in a few hours.[73] A similar phenomenon (*i.e.*, quick saturation of sulfur poisoning) was also observed by other researchers[79–82] with much lower H_2S concentration (*e.g.*, 0.1 to 1 ppm).

However, some other studies show that, in addition to the initial quick poisoning effect, the cell power output continues to degrade with a much slower but still significant rate (usually in an almost linear way) for a long period of time. Zha *et al.*,[54] Sprenkle *et al.*,[57] and Ishikura *et al.*[58] named this continued degradation *2nd stage slower poisoning*. Within this category, there are also two different scenarios. Some studies show that the *2nd stage slower poisoning* reaches saturation after some time,[11] while others show continued degradation that lasts for hundreds or even thousands of hours without showing any signs of reaching saturation.[52,54,61,82–84]

It is not clear what causes such *2nd stage slower poisoning* that lasts for a very long time. It would certainly be difficult to explain from the sulfur adsorption point of view. Bulk sulfidation of either Ni or YSZ also seems unlikely as they are thermodynamically unfavorable, especially for those studies using only low ppm of H_2S.[52,57,58,61,83] It is unlikely due to the degradation of other cell components since the drop in performance usually appears to be much more severe than those observed in fuels without sulfur.[54,57,58] On the other hand, the study by Hagen and co-workers suggests that the loss of the Ni-percolation network near the anode–electrolyte interface was observed for the Ni-YSZ anode in H_2S-containing fuels under large polarization conditions, which also display 2nd stage degradation for hundreds of hours.[84]

Recently, the study by Yang *et al.* shined some light upon the possible origins for the *2nd stage slower poisoning*.[82] Using anode-supported button cells with Ni-YSZ anode and LSCF cathode, Yang observed that button cells sealed with different sealants showed different *2nd stage* behavior: for example, at 750 °C in a fuel with 1 ppm pH_2S/pH_2 under a constant current density of 200 mA cm^{-2}, cells sealed with the Ceramabond® 552 (C552) sealant showed *2nd stage slow degradation* that lasted for ~1000 h without any signs of saturation. In contrast, cells sealed with the G-18 (from Pacific Northwest National Lab, PNNL) sealant seemed to reach saturation right after the quick poisoning stage and showed no *2nd stage slow degradation*. This indicates that the previously reported *2nd stage slow degradation* is unlikely the inherent behavior of a Ni-YSZ anode but rather associated with other complications. Two possible explanations are as follows. First, it is possible that the anodes were contaminated by some detrimental elements in the C552 sealant, which interact

Table 3 Summary of the studies involving long-term sulfur poisoning tests for solid oxide fuel cells

References	Cell/stack structure	T/°C	Fuel utilization (%)	j/mA cm^{-2}	pH_2S/pH_2 (ppm)	Observations about the *2nd stage slow poisoning*	
						Time/h	Reached saturation?
Feduska and Isenberg[73]	7 cathode supported tubular cell stacks	1000	N/A	150	333–1000	Not observed for 800 h	
Iritani *et al.*[81]	22 cathode supported tubular cell stacks	900	60%	200	1	Not observed for 530 h	
Batawi *et al.*[80]	5-cell stack	950?	N/A	200	100	Not observed for 450 h	
Maskalick *et al.*[79,83]	Single cathode supported tubular cell	1000	85%	350	0.1	Not observed for 500 h	
		1000, 1025	85%	350	1	1500	No
		1000	N/A	350	5	450	No
Singhal *et al.*[52]	Cathode-supported?	1000	N/A	250	10	80	No
Trembly *et al.*[11]	Single electrolyte-supported cell[a]	850	40%[b]	200	837	450	Yes
Sprenkle *et al.*[57,68]	Single anode-supported button cell	750	N/A	1100[c]	0.1, 1, 10	200	No
Zha *et al.*[54]	Single electrolyte-supported button cell	800	<5%[b]	250[c]	2	24	No
		800	<5%[b]	250[c]	100	120	No
Yang *et al.*[82]	Single anode-supported button cell	750	<5%	200–800	1–10	1000[d]	No
		750	<5%	200–400	1–11	Not observed for 3000 h[e]	
Hagen *et al.*[84]	Single anode-supported cell	850	<32%[b]	1000	15	500	No

[a] Ni-GDC anode. [b] Estimated fuel utilization value. [c] Initial current density under constant voltage conditions. [d] Using the Ceramabond® 552 sealant. [e] Using the G-18 sealant.

unfavorably with H_2S, leading to continuous poisoning of the anode, while the G18 sealant does not have such detrimental elements. Second, the cathode performance may be adversely affected by a small leakage of H_2S from the anode side through the C522 sealant while there was no leakage of H_2S through the G18 sealant.

2.2.8. Reversibility of sulfur poisoning. Upon removal of H_2S from the fuel, both complete recovery[27,52–54,58,73,79,85,86] and partial recovery of power outputs[11,54,58,61,81,87,88] have been observed. Cell failure is rare, but still observed sometimes.[53,89] From a thermodynamic point of view, sulfur poisoning should be reversible when the concentration of sulfur in the fuel is sufficiently low. In reality, however, other factors such as contamination from other cell components (*e.g.*, sealant) and microstructural changes (due to coarsening of porous electrodes) may also influence the observed electrochemical behavior. For example, it has been reported that terracing increases on nickel surface upon exposure to H_2S-containing fuels.[90] It is still not clear, however, how these microstructural changes influence the electrochemical poisoning behavior. Nevertheless, the general trend is that sulfur poisoning tends to be more reversible at a higher operating temperature, in a lower H_2S concentration, and for a shorter period of exposure to H_2S.

3 Behaviors of alternative anode materials in sulfur-containing fuels

Because of the vulnerability of Ni-YSZ cermet anodes to sulfur contaminants, various alternative materials or material combinations have been studied as potential SOFC anodes for improved sulfur tolerance. In this section, the alternative anode materials are summarized with a particular focus on their electrochemical behavior upon exposure to sulfur-containing fuels. Since a number of previous publications have described the detailed behavior of many individual materials,[33–35,91] the focus of this section will be on the *general features* for different types of materials and our perspectives on these materials.

3.1. Ni-YSZ cermet anodes with incorporation of other materials

Because of the superior electrochemical performance of Ni-YSZ cermet anodes in sulfur-free fuels, various approaches have been explored to modify Ni-YSZ cermet anodes *via* incorporation of other materials in an effort to achieve improved sulfur tolerance while maintaining excellent performance. For example, Singhal *et al.* reported impregnation of Ni-YSZ cermets with various oxides including doped ceria and B-site doped strontium titanium oxide ($SrTi_{1-x}M_xO_3$), as well as high surface area nickel and cobalt metal precursors.[52] Later, Sasaki *et al.* studied the behavior of Ni-YSZ anodes in sulfur-containing fuels modified with different materials including CeO_2, Y_2O_3, La_2O_3, MgO, Nb_2O_5, Sc_2O_3, ZrO_2, TiO_2, Ru, CaO, Co, and Al_2O_3 prepared by impregnation.[53] Kurokawa *et al.*[89] and Yun *et al.*[92] also decorated Ni-YSZ cermet with CeO_2 and/or samaria doped ceria (SDC) *via* an infiltration process, while Smith and McEvoy infiltrated pre-reduced porous Ni-YSZ cermet anode with ammonium metatungstate.[93,94] Very recently, Marina *et al.* incorporated Sn and Sb into the Ni-YSZ anode through *in situ* vapor phase deposition.[95]

Unfortunately, except for a few selected cases, most of the modified Ni-YSZ anodes *via* incorporation of foreign materials still display the typical poisoning behavior when ppm-level H_2S is introduced into the fuel stream.[52,53,89,92] Although many of such modified Ni-YSZ anodes are *claimed* to have improved sulfur

tolerance over the conventional Ni-YSZ anode (based on observation of a smaller relative drop in power output due to sulfur poisoning ΔP_r), the rapid initial degradation seems to be still unavoidable. It appears that the insufficient sulfur tolerance for most of these modified Ni-YSZ anodes originates from the difficulties in depositing uniform coatings with *proper coverage* of the porous anode surfaces. On the other hand, electron pathways may be blocked when these materials form a continuous dense film on Ni. The challenge is how to enhance sulfur tolerance without affecting other useful properties of Ni-YSZ anodes by some innovative surface modification,[96] as was done for enhancing tolerance to coking of Ni-YSZ anodes.[2]

In addition, alternative sulfur-tolerant anode materials like $Sr_{0.8}La_{0.2}TiO_3$ (SLT)[97] have also been used to replace the outer layer of a Ni-YSZ support for anode-supported cells. In a fuel with pH_2S/pH_2 of 100 ppm, such a modified cell still experienced a rapid initial voltage drop, but the *2nd stage slower poisoning* as observed in the control cell with the Ni-YSZ anode support seems to be prevented. The rapid initial degradation indicates that the SLT anode support over the thin Ni-YSZ anode could not remove the sulfur in the fuel as an outer catalyst nor eliminate the sulfur adsorption on Ni, and the mechanism for preventing the long-term slow degradation is not clear.

3.2. Ni-based cermet anodes with YSZ replaced by other oxygen ion conductors

The YSZ phase in Ni-YSZ cermet anodes has been replaced by other oxygen ion conductors in an effort to enhance sulfur tolerance. For example, Sasaki and co-workers studied Ni-scandia stabilized zirconia (Ni-ScSZ) anode[53] while others studied Ni-gadolinia doped ceria (Ni-GDC) anode.[11,98–100] While the relative drops in power output ΔP_r for SOFCs with Ni-SSZ or Ni-GDC anodes were reported less than those with Ni-YSZ anodes, the sulfur poisoning characteristics remain similar in many cases.

First, both Ni-SSZ and Ni-GDC anodes were still sensitive to the same low level of H_2S as Ni-YSZ, as evidenced by the rapid drop in cell power output upon exposure to low ppm-level H_2S contaminants.[53,100] The anode polarization resistance also increased dramatically: for example, the interfacial resistance of a Ni-GDC anode increased from to 0.55 to 0.75 Ohm cm^2 (36% increase) upon exposure to 5 ppm H_2S at 800 °C.[100] Similarly, the polarization resistance of a Ni-GDC anode increased dramatically upon exposure to 0.5 ppm H_2S at 715 °C.[101] (However, it was reported by Ouweltjes *et al.* that, at 900 °C, the Ni-GDC anode showed no poisoning effect by H_2S of up to 9 ppm, although it is not clear what caused the difference in behavior.[98,99])

Second, the observed ΔP_r is still too large to be negligible although it maybe smaller than that for Ni-YSZ. In the study by Sasaki *et al.*, 100 ppm H_2S led to a ΔP_r of ~25% at 800 °C for the Ni-ScSZ anode at a current density of 200 mA cm^{-2}. In fact, the observed difference in ΔP_r for those anodes *versus* Ni-YSZ may have more correlations with cell fabrication and electrochemical testing conditions than intrinsic sulfur poisoning behavior.

Third, in terms of the poisoning mechanism, sulfur is still expected to adsorb at the nickel surface and along the triple phase boundary (TPB),[102] which blocks the active sites for fuel oxidation (see Section 5). Faster oxygen ion conduction might enhance sulfur removal, but there is no viable mechanism for such anodes to significantly reduce or fully eliminate the sulfur poisoning process, given that it has been shown in Section 2.2.3 that increasing the cell current density under small bias conditions does *not* have much impact on the real extent of sulfur poisoning.

3.3. Cermet anodes with Ni replaced by other metals

Similarly, the Ni phase in Ni-YSZ cermet anodes can also be replaced by other metals that have lower affinity for sulfur. However, it is not trivial to find metals or alloys that have adequate catalytic activity and less affinity towards sulfur adsorption. For example, Singhal and others discussed the potential for cobalt and platinum[52,103] as the metal phase in the cermet anode, and concluded that they are still subject to sulfur poisoning due to the high affinity of those metals for adsorbed sulfur.

On the other hand, it is well known that copper and silver have much less affinity for sulfur adsorption: the free energy change for sulfur adsorption on copper and silver is significantly more positive than those for sulfur adsorption on nickel and cobalt. (See the summary in references like ref. 65.) For example, the heat of sulfur adsorption (enthalpy) at a surface coverage of 0.5 (number of adsorbed sulfurs/number of saturated sulfurs per unit area = 0.5) is about −160 kJ mol^{-1} for Ni, while it is only about −80 kJ mol^{-1} for Cu. As a result, at a temperature of ~750 °C the equilibrium pH_2S/pH_2 value for the same level of the sulfur surface coverage is $\sim 10^4$ *times higher* for sulfur on Cu than on Ni. (Assuming comparable entropy change for the dissociative adsorption process, then,

$$\frac{pH_2S_c^{Cu}/pH_2}{pH_2S_c^{Ni}/pH_2} = \exp\left(\frac{\Delta H_s^{Cu} - \Delta H_s^{Ni}}{RT}\right) = \exp\left(\frac{(160-80)\times 10^3 \text{ J mol}^{-1}}{8.314 \times 1023 \text{ J mol}^{-1}}\right) \approx 1.2 \times 10^4.)$$

Since the Ni-YSZ anode interfacial resistance starts to degrade when pH_2S/pH_2 is 0.05 ppm at 750 °C,[27] the above calculation suggests that to reach a similar surface coverage of sulfur on Cu would require pH_2S/pH_2 of $0.05 \times 10^4 = 500$ ppm. This estimation correlates well with the experimental data reported by He *et al.* for a Cu-ceria-YSZ cermet anode prepared by infiltration of a YSZ anode skeleton first by Cu and then by CeO_2 precursor solutions: the cell maintained stable power output until the pH_2S/pH_2 was increased to ~450 ppm and above.[104] It is interesting to note that He *et al.* also showed that cerium oxide starts to react with H_2S at a concentration of 450 ppm H_2S and above. The incorporation of ceria into the Cu-based anode is also reported to solve the problem of low catalytic activity for Cu.[14,104,105] Unfortunately, some practical issues still remain for such Cu-ceria-YSZ cermet anodes with superior sulfur tolerance: the low melting point of Cu and copper oxides makes it difficult to fabricate anode-supported cells using conventional co-firing methods, and the relatively low cell performance and limited long-term stability hinder its practical application.

Another example in this category is the Ni–Mo alloy-based anode explored by Choi *et al.*[106] Ni–Mo and Ni–Mo–CeO_2 were infiltrated into YSZ scaffolds *via* wet-impregnation of Ni, Mo, and CeO_2 precursors. Although the cells based on these anodes suffered from initial quick poisoning when 50 ppm H_2S was introduced into the fuel stream, they showed an interesting feature: the cell power output actually increased gradually to the level before poisoning upon continued exposure to fuels with 50 ppm H_2S for ~6 days under a constant cell voltage of 0.5 V.

3.4. Conductive oxide anode materials

Anodes based on *nickel-free* conductive metal oxides are perceived to hold potential for solving the problems associated with Ni-based cermet anodes: susceptibility to deactivation by impurities like sulfur and destruction by re-oxidation and carbon deposition in hydrocarbon fuels. Accordingly, many metal oxides of different structures and compositions have been studied as potential SOFC anode materials for improved sulfur tolerance.[33–35] For example, Marina *et al.* and Mukundan *et al.* studied perovskite-structured $Sr_{1-x}La_xTiO_3$ (LST, in particular x = 0.3–0.4),[77,107–110] and Kurokawa *et al.* studied Y-doped $SrTiO_3$.[111] Winnick and co-workers[112–116] and Cooper *et al.*[117] studied perovskite-structured $La_{1-x}Sr_xVO_3$ (LSV, in particular, $x = 0.3$), while Danilovic *et al.* studied $Ce_{0.9}Sr_{0.1}VO_x$ (x = 3, 4) and its doped variations.[118,119] Zha *et al.* studied perovskite-structured $La_{1-x}Sr_xCr_{1-y}Mn_yO_3$ (LSCM, in particular, $x = 0.25$, y = 0.5)[120] and pyrochlore-structured $Gd_2Ti_{2-x}Mo_xO_7$ (in particular, $x = 0.6$).[121,122] Huang *et al.* studied double-perovskite-structured $Sr_2Mg_{2-x}Mo_xO_6$ (SMMO, in particular, $x = 1$),[123,124] and Xiao *et al.* studied $Sr_2Fe_{4/3}Mo_{2/3}O_6$.[125] Except for $Sr_2Mg_{2-x}Mo_xO_6$ that uses $La_{1-x}Sr_xGa_{1-y}Mg_yO_{3-\delta}$ (LSGM, in particular, x = 0.2, y = 0.17, δ = 0.185) electrolyte, all other studies are based on the YSZ electrolyte. Lu *et al.* studied combination of conductive oxide anode with impregnation of metal catalyst like Pd.[126] Buffer layers (also referred to as interlayer) are commonly applied between anode and electrolyte because of their limited chemical and thermal compatibilities. For example, $La_{0.4}Ce_{0.6}O_{2-\delta}$ and $Ce_{0.8}Gd_{0.2}O_{2-\delta}$ interlayers are used for SMMO[124] and LSCM[127] anodes, respectively.

However, the number of studies on any *single* material is usually very limited and the conditions under which the materials are investigated (*e.g.*, in terms of temperature, pH_2S/pH_2, and polarization) are very narrow, which make the evaluation of their true potential difficult. Because individual properties and behavior upon exposure to sulfur-containing fuels have been enumerated in earlier publications,[33,35] they will not be repeated here. Instead, we would like to discuss some features that are commonly observed in these studies.

•**Improved sulfur tolerance.** It seems fair to state that many of those conductive oxide materials *do* display improved sulfur tolerance: the critical pH_2S/pH_2 ratio above which sulfur poisoning becomes significant is usually *higher* than for the Ni-YSZ anode. For example, $La_{0.35}Sr_{0.65}TiO_3$–$Ce_{1-y}La_yO_2$ composite anode shows *no* increase in anode polarization resistance when the pH_2S/pH_2 is 7.8 ppm at 750 °C,[108] compared to ~0.02 ppm for the Ni-YSZ anode.[27] For $La_{0.8}Sr_{0.2}Cr_{0.8}Mn_{0.2}O_3$ (LSCM) anode, at 1000 °C, 10 ppm H_2S also does not cause noticeable sulfur poisoning,[110] while 2 ppm H_2S leads to poisoning for the Ni-YSZ anode.[27]

However, oxide anodes usually experience sulfur poisoning when higher concentration of H_2S is present in the fuels. For the $La_{0.35}Sr_{0.65}TiO_3$–$Ce_{1-y}La_yO_2$ composite anode, at higher pH_2S/pH_2 concentrations like 30.9 ppm at 800 °C or 1055 ppm at 850 °C, it does show the typical sulfur poisoning behavior with a sharp drop in the cell power output and increase in the anode overpotential once H_2S is introduced into the fuel.[77,108,109] A similar case happens to the $La_{0.8}Sr_{0.2}Cr_{0.8}Mn_{0.2}O_3$ (LSCM) and $Sr_2Fe_{4/3}Mo_{2/3}O_6$ anode: 100 ppm and higher H_2S leads to dramatic increase in anode overpotential.[110,120,125,128] Even for the highly promising $Sr_2MgMoO_{6-\delta}$ (SMMO) anode, the increase in anode overpotential is much more obvious when the H_2S concentration is 50 ppm than 5 ppm.[124]

It is hypothesized that reduction of sulfur adsorption on oxide anode materials contributes to the enhanced sulfur tolerance. For example, Marina *et al.* showed that for $La_{0.35}Sr_{0.65}TiO_3$–$Ce_{1-y}La_yO_2$ anode at 850 °C, the calculated surface coverage by absorbed sulfur is only 0.5 at 75 ppm and 0.9 at 750 ppm.[77] In comparison, for the Ni-YSZ anode, the sulfur surface coverage is already close to saturation at below 10 ppm.[66] (Also see Section 5.)

•**Sulfur-enhancement effect.** As opposed to sulfur poisoning, studies also show some oxide anode materials actually display *sulfur enhancement* effect: *i.e.*, cell electrochemical performance would increase upon exposure to very *high concentration of H_2S* (in the percentage range) at high temperatures (*e.g.*, 850–1000 °C). For example, Mukundan *et al.* reported that the cell power output *increases* for the $La_{0.35}Sr_{0.65}TiO_3$–YSZ composite anode when 5000 ppm (0.5%) H_2S was introduced into the fuel with a composition of 86.4% H_2/3.6% H_2O balanced by Ar at 1000 °C. Similarly, $La_{0.7}Sr_{0.3}VO_3$ anode displays lower interfacial resistance in 3–10 vol% H_2S balanced by H_2 than in pure H_2,[114,115] and $Gd_2Ti_{1.4}Mo_{0.6}O_7$ (GTMO) displays a maximum powder density of 340 mW cm^{-2} in a fuel mixture of 10% H_2S/90% H_2, while P_{max} in pure H_2 is only 225 mA cm^{-2}.[122] The fundamental reason for such *sulfur enhancement* is not clear at this moment, but we hypothesize that the transition of the material's surface from oxide to a very *thin* (2D) layer of conductive sulfides upon exposure to the high concentration of H_2S might contribute to the enhancement. Such hypothesis is consistent with the limited experimental evidence: for example, the presence of Raman peaks corresponding to MoS_2 has been identified on the surface of GTMO anode after exposure to 10% H_2S/90% H_2, even though the bulk GTMO material remains intact according to X-ray diffraction (XRD).

•**Seemingly conflicting data.** There are also some seemingly conflicting results in the literature regarding the behavior of certain conductive oxide materials as alternative SOFC anodes in sulfur-containing fuels. For example, Marina *et al.* reported that the $La_{0.35}Sr_{0.65}TiO_3$–$Ce(La)O_2$ composite anode displays large drop in cell power output upon exposure to a fuel with pH_2S/pH_2 of 1055 ppm at 850 °C, while Mukundan *et al.* reported that a similar $La_{0.35}Sr_{0.65}TiO_3$–YSZ composite anode did not show an increase in overpotential when pH_2S/pH_2 was 1000 ppm at 1000 °C; they reported an *enhancement* in performance when

pH_2S/pH_2 was 5000 ppm. Another example is $La_{0.7}Sr_{0.3}VO_3$: although *sulfur enhancement* was observed in 10% H_2S/90% H_2 at 950 °C by Aguilar *et al.*,[114] the study by Peng *et al.* shows the addition of 0.5% H_2S to H_2 fuel causes the total cell interfacial resistance to increase dramatically at 800 °C.[129] It is not clear whether such discrepancies are due to the nature of the sulfur–anode interactions in different regimes (in terms of H_2S concentration and temperature) or due to some other unidentified difference in experiments.

•**Drawbacks of conductive oxide anodes.** The limitations of conductive oxide anodes include low electrical conductivity (compared with Ni), poor catalytic activity toward fuel oxidation, and inadequate compatibility with the electrolyte (or other cell components) at high temperatures during fabrication. These disadvantages severely hinder their applicability to practical applications.

The electrical conductivity for most of these conductive oxide anode materials is invariably lower than that of the Ni-YSZ anode, leading to high anode resistance and poor performance.[130] For example, at 800 °C in fuel atmosphere (pO_2 of $\sim10^{-15}$ to 10^{-22} atm), anode bulk conductivity (*i.e.*, with low porosity) is $\sim$1 S cm^{-1} for $La_{0.75}Sr_{0.25}Cr_{0.5}Mn_{0.5}O_3$[120,127] and $Gd_2Ti_{1.4}Mo_{0.6}O_7$,[122] $\sim$10 S cm^{-1} for $Sr_2MgMoO_{6-\delta}$ (SMMO),[124] $\sim$10 to 100 S cm^{-1} for $La_{0.35}Sr_{0.65}TiO_3$,[107,131] and $\sim$100 S cm^{-1} for $La_{0.7}Sr_{0.3}VO_3$.[115] In lab experiments, such low conductivity still allows high power density since a metal mesh and paste (usually platinum or nickel) are normally applied above the anode as current collectors.[35] In some cases, in fact, the platinum or nickel may penetrate into the porous anode, making it difficult to figure out the *actual* role of the platinum or nickel used as a current collector. In search for new alternative anode materials to replace Ni-YSZ, therefore, it is vital to ensure that the metal paste used as a current collector does not penetrate into the porous anode and come in close contact with the electrolyte. Otherwise, such current collectors may serve as part of the functional anode, thus complicating the observed sulfur–anode interactions. In real fuel cell stacks, the nickel mesh/paste may be used as current collectors; however, the reliability of this current collector is still questionable since the susceptibility of Ni to sulfur and other contaminants (like carbon) still remains. In particular, the low electrical conductivity of oxide anodes may pose an even greater problem if the anode-supported cell structure is to be adopted.

In addition, it is difficult for most of the ceramic anode materials to be adopted in the state-of-the-art SOFC fabrication processes based on the YSZ electrolyte, especially for an anode-supported cell structure that has the best performance and long-term stability. The difficulties originate usually from alternative anodes' limited physical, chemical, and/or thermal compatibility with the YSZ electrolyte during fabrication at high temperatures. For example, both $La_{0.7}Sr_{0.3}VO_3$ and $Gd_2Ti_{1.4}Mo_{0.6}O_7$ anodes were processed in reducing atmosphere at elevated temperatures,[115,122] which is not very compatible with current processes and pose challenges for the preparation of cathode materials.

3.5. Metal sulfide anode materials

Various metal sulfides have been studied as potential anode materials for SOFCs, particularly those targeted towards direct utilization of high concentration (*e.g.*, on the percentage level or higher) of the H_2S fuel.[33–35,78,132–147] Although some of them seem to show decent performance in those high sulfur concentration fuels, there is little information on long-term stability of these materials, due partially to the highly poisonous and corrosive nature of H_2S at high concentrations. Also, metal sulfides tend to decompose back to metals when the relative H_2S concentration is low: For example, at 1000 K, Ni_3S_2 will decompose when $pH_2S/pH_2 < \sim3 \times 10^3$ ppm (0.3%), while MoS_2 with a higher melting point will decompose when $pH_2S/pH_2 < 3 \times 10^2$ ppm. Such instability in fuels with low concentration of sulfur suggests that they may not be suitable for typical SOFCs to be powered by fuels with low concentration (tens of ppm or lower) of sulfur. Thus, metal sulfide anodes will not be discussed here in detail. Interested readers are referred to previous reviews and the cited references.

3.6. Electrochemical characterizations of sulfur–anode interactions

To conclude the sections on the behaviors for alternative sulfur tolerant anodes as well as conventional Ni-YSZ cermet anodes, we present our perspectives about cell configuration and techniques for electrochemical characterizations of SOFC button cells.

3.6.1. Cell configuration. The best cell configuration for evaluating sulfur–anode interactions is electrolyte-supported button cells with relatively thick electrolytes and properly positioned reference electrodes, as schematically shown in Fig. 3, which enables separation of the anode process from that of the cathode and real time monitoring of the anode performance. In contrast, it is very difficult to do the same on an anode-supported cell with an electrolyte thickness of only $\sim$10 μm.[148,149] Attempts to do 3-electrode measurements on such a cell may result in substantial errors in estimation of half-cell overpotential unless the reference is placed in a very special way.[51] Accordingly, for anode-supported cells, the relative changes in cell voltage or current density were measured to characterize indirectly the electrochemical behavior of the Ni-YSZ anode in H_2S-containing fuels.

Symmetrical cells with two identical anodes are also employed in some studies.[70] However, the interpretation of the data would be more complicated as cathodic reduction of water is involved in one of the electrodes. Without a reliable reference electrode, it would be difficult to correctly interpret the data and to gain insight into fuel cell operation.

3.6.2. Preferred electrochemical measurements. For mechanistic investigation of the anode–sulfur interactions or characterization of alternative anode materials, in our opinion, the most important measurement is *impedance spectroscopy* (*IS*), which can be acquired before and after exposure to sulfur poisoning. Preferably, the impedance spectra of the anode/electrolyte interface would be directly measured if the anode and the cathode could be separated *via* proper placement of a reference electrode using three- or four-electrode configuration. Even under a two-electrode configuration, impedance spectra are still informative. The change in impedance spectra provides valuable

information about the impact of sulfur poisoning on both bulk resistance and anode (or cell) polarization resistance, which influence how sulfur–anode interactions are interpreted. Taking the Ni-YSZ cermet anode as an example, the initial quick poisoning by low concentration (ppm-level) H_2S leads to large increase in anode interfacial resistance but not bulk resistance.[27,54,55,58,100,150] This is in good agreement with the mechanism of sulfur adsorption on the nickel metal surface as the bulk resistance is determined by the electrolyte and the electrode ohmic resistance, which are not expected to change by a surface adsorption process. However, as stated, some researchers have also observed *2nd stage slow degradation* after the rapid initial poisoning. In that case, cells tend to show small gradual increase in bulk resistance together with continued increase in anode (cell) interfacial resistance.[58,84] A step further in sulfur poisoning is cell failure, which is accompanied by a very large increase in bulk resistance as well as interfacial resistance.[58] Such information would help clarify the interaction process, and is less straightforward to obtain from other measurements like anode polarization curves (overpotential *versus* current density) even with a properly positioned reference electrode. Other benefits for impedance spectra include (i) the anode polarization resistance under open circuit conditions could be used to extract anode exchange current density, j_0, which reflects the intrinsic change in electrode kinetics caused by sulfur poisoning as discussed before, and (ii) the frequency information embedded in impedance spectra could be used to shine light on the impact of sulfur on the individual processes like charge transfer and mass transfer.

In addition to impedance spectroscopy, other valuable cell performance measurements include measuring current–voltage (*I–V*) curves and continuous monitoring of cell power output *versus* time, preferably under constant current conditions (*P–t*). The *I–V* curves provide direct representation of cell performance and information about the impact of polarization on the observed powder output drop due to sulfur poisoning ΔP_r,[55,57] while continuous monitoring of cell power output provides information about the overall stability of the cell and real-time change in cell power output as H_2S is introduced or removed from the fuel. Both the magnitude and the rate for the change in ΔP_r would be of interest from a theoretical point of view. For example, the rate of degradation due to sulfur adsorption would, in principle, be much faster than that due to formation of bulk sulfides.

It is recognized that many new materials used as anodes have not yet been optimized for cell stability, and cells with those materials degrade in sulfur-free fuels. However, even in those cases, continuous monitoring of cell power output *versus* time is still valuable if the experiment could be kept short to within a few hours or tens of hours.

It is noted that neither *I–V* nor power output *versus* time (*P–t*) measurements should be used to replace impedance data and *vice versa*. This is because both *I–V* and *P–t* may be influenced by many factors other than the anode process. An extreme example is that even the Ni-YSZ anode would display a very small power output drop of 1% when it is tested under a small constant current density of ~20 mA cm^{-2} exposed to 11 ppm H_2S at 750 °C (see Fig. 7) while we know that 11 ppm H_2S will cause the anode polarization resistance to more than double.[27,54] Therefore, the authors would encourage future research to provide all above measurements (*IS*, *I–V*, and *P–t*), which would help clarify the reaction mechanism and compare data from different sources. Other electrochemical measurements that may appear in the literature for characterizing sulfur–anode interactions include anode polarization curves and monitoring of anode overpotential *versus* time, which also provide some useful information.

3.6.3. Proper representation of sulfur–anode interactions. In the SOFC literature, definitions such as *sulfur poisoning* or *extent of sulfur poisoning* are used and even compared often without being defined clearly. To avoid confusion, we recommend using the relative change in anode exchange current density or the relative change in anode polarization resistance *under open circuit conditions* as the most direct representation of the *extent of sulfur poisoning* due to their (relatively) intrinsic nature and independence of testing conditions.

Other measured quantities, such as relative voltage drop at a constant current or relative current drop at a constant voltage, may reflect in a certain way the changes in anode performance upon exposure to sulfur, but should be clearly stated and treated with care: although they do reflect sulfur poisoning, their values depend on other factors like cathode and electrolyte contributions and how the electrochemical measurements are conducted. Thus, it is *not* recommended to determine which anode is more or less sulfur tolerant based on the numbers like ΔP_r due to sulfur poisoning for different anodes under different operating conditions.

Another important factor in terms of evaluating sulfur tolerance is the critical sulfur concentration at which sulfur poisoning obviously starts. It is realized that the critical value might be difficult to be determined in experiments. Therefore, reporting the sulfur poisoning behavior under the lowest sulfur concentration available is also desirable.

4 Chemical and microscopic characterizations

Various *ex situ* and *in situ* experimental techniques have been employed for characterization of chemical composition (surface species and new phases), morphology, and microstructure of anodes exposed to sulfur-containing fuels. This section will provide an overview of the techniques employed, the observations made, and the implications.

4.1. *Ex situ* and *in situ* characterizations

In a typical *ex situ* measurement, the sample is characterized *after* it has been exposed to a sulfur-containing fuel at elevated temperatures or tested in a fuel cell under practical operating conditions. After exposure to H_2S, the sample has to be cooled down to room temperature, taken out from the testing apparatus, and transferred into a characterization chamber for analyses. Typical characterization methods include X-ray diffraction (RXD) and X-ray adsorption spectroscopy (XAS), electron microscopy (SEM, TEM, and STEM), electron spectroscopy (EDX, XPS, AES, and EELS), low energy electron diffraction (LEED), mass spectrometry (MS), and vibrational spectroscopy (IR and Raman). For surface characterization, careful preservation of the sample surface in the process of transferring

a sample from a testing apparatus (at high temperature in a fuel containing sulfur) to an analysis chamber is *as important as* the characterization itself because improper sample transfer may introduce artifacts. Since SOFCs are typically operated at high temperatures, it is impossible to preserve the exact same conditions (temperature and atmosphere) on the sample surface when the examination of the sample is performed at room temperature. Just cooling a Ni-YSZ sample from high temperature to room temperature in a H_2S-containing fuel may create uncertainties or even erroneous information, as to be shown in the next section for Ni-YSZ anodes.

For *in situ* characterization, in contrast, the sample is placed in a temperature- and atmosphere-controllable chamber accessible to probing stimulus and signal detector of the characterization equipment. At elevated temperatures in a designated atmosphere, signals from a sample under electrochemical operation can be collected in real time. While electron microscopy and spectroscopy offer the highest spatial resolution and sensitivity in identification of structure, morphology, and composition of materials, it is very difficult, if not impossible, to apply these techniques for *in situ* characterization of the sulfur poisoning processes. The main challenge is the degree of vacuum required for electron-based techniques. Thus, the most powerful *in situ* techniques for the study of the sulfur poisoning process are vibrational spectroscopy (especially Raman) and X-ray analyses (XRD and XAS). Schematically shown in Fig. 9 is the arrangement used for the *in situ* Raman spectroscopy study of anode materials.[56,62] The readers are also referred to the review by Pomfret *et al.*[151] about other *in situ* characterization techniques used for SOFC anode studies.

The advantages of *in situ* over *ex situ* characterization are obvious: it can provide first hand information on the interactions of sulfur species with anode materials under conditions similar to real SOFC operation, thus avoiding complications associated with sample transfer. Further and in particular, the most unique advantage of *in situ* characterization is the possibility for direct correlation between different measurements performed at the same time. For instance, surface species (*e.g.*, reaction intermediates) or new phases identified by Raman spectroscopy may be linked directly to electrode polarization as determined from electrochemical measurements (*e.g.*, impedance spectroscopy) and to the chemical environment the sample is experiencing as probed by mass spectrometry, thus providing valuable information vital to unraveling the mechanism of electrode reactions.

4.2. Microstructural and chemical changes during sulfur–anode interactions

4.2.1. Ni-YSZ cermet anodes. Table 4 summarizes studies on the characterization of Ni-YSZ cermet anodes upon exposure to H_2S-containing fuels. The following observations are made. First, the interactions between H_2S and Ni-YSZ anodes at typical SOFC operating temperatures (~550 °C and above) in fuels with *low ppm-level* H_2S do *not* lead to bulk nickel sulfide formation nor morphology changes. By using *in situ* Raman microspectroscopy, Cheng and Liu found that at ~570 °C in a fuel with pH_2S/pH_2 of 100 ppm, *no* bulk nickel sulfides were identified on the Ni-YSZ surface, and *no* changes in surface morphology were observed even after a prolonged exposure.[56] Such observation is consistent with the several carefully controlled *ex situ* experiments in which no bulk sulfides nor morphology changes have been detected.[52,61,152] It is concluded that the nickel-YSZ cermet anode poisoning by low concentration H_2S at elevated temperature (*e.g.*, ≥~550 °C) is *not* caused by bulk nickel sulfide formation. Instead, it is caused by rapid adsorption of elementary sulfur on the Ni surface, as evidenced from the observed fast poisoning process, the sensitivity to sub-ppm-level H_2S (see Section 2.2.6),[27] and from theoretical calculations, as to be discussed later in Section 5.[66]

It has been reported that bulk nickel sulfides (*e.g.*, Ni_3S_2) and/or dramatic morphology changes for the post-sulfur exposure samples were observed even though the sulfur concentration (pH_2S/pH_2) was on the order of hundreds of ppm or even lower.[11,86,153,154] For example, Dong *et al.* identified bulk Ni_3S_2 and Ni_3S_4 on the Ni-YSZ cermet after exposure to the fuel with pH_2S/pH_2 of 100 ppm at 727 °C for 5 days and *cooled down with the furnace in the same fuel*.[153,154] Similarly, Trembly *et al.* identified sulfur in the percentage level in the anode after testing in a fuel with pH_2S/pH_2 of 590 ppm at 750 °C.[11]

The discrepancy between the first two observations stems from the complications that occurred when the samples went through the changes in temperature and atmosphere during the sample transfer process, as has been clearly illustrated in the study by Cheng and Liu.[56] In that study, for the *ex situ* characterization, Ni-YSZ cermet was exposed to a fuel with $pH_2S/pH_2 = 100$ ppm at 800 °C for different durations (2 to 48 h). Afterwards, the samples were then *cooled down slowly* (~3 °C min^{-1}) to room temperature *with the samples being exposed to the same fuel* (*i.e.*, with $pH_2S/pH_2 = 100$ ppm during cooling), and various nickel

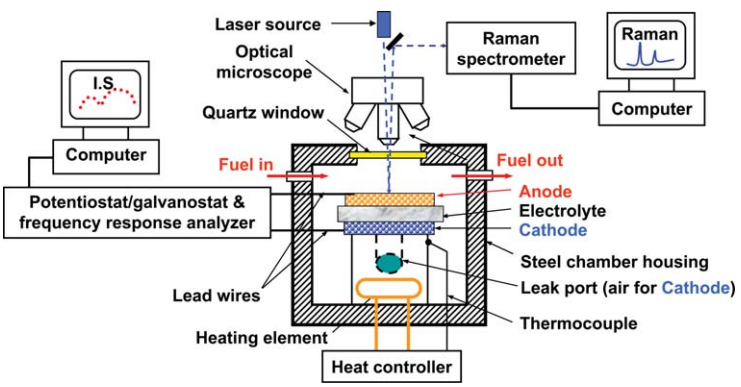

Fig. 9 Schematic for the *in situ* Raman microspectroscopy measurement system that is coupled with electrochemical measurement equipment.

Table 4 Summary of *ex situ* and *in situ* characterizations of anode materials after interactions with sulfur-containing fuels under various conditions

References	Anode	Technique	T/°C	pH_2S/pH_2 (ppm)	*In situ* or *ex situ*	Sample details	Observations
Singhal *et al.*[52]	Ni-YSZ	SEM/EDX, photometric	900–1000	10	*Ex situ*	After poisoning and regeneration	No sulfur observed after regeneration
Waldbillig *et al.*[61]	Ni-YSZ	SEM/EDX, EM/EDX	750	0.1–10	*Ex situ*	Cells fully poisoned and fully regenerated	No sulfur or additional bulk phases (other than Ni and YSZ) detected
Sasaki *et al.*[53]	Ni-YSZ, Ni-SSZ	XPS, SEM/EDX	800	5–100	*Ex situ*	After poisoning, the sample was *rapidly* cooled in N_2	The presence of sulfur was identified by XPS, Ni oxidized to NiO for cells that suffered irreversible voltage drop
Trembly *et al.*[11]	Ni-GDC	SEM/EDX, XPS	750	590	*Ex situ*	After cell testing for 580 h in the fuel with H_2S	Morphology change observed, the significant presence of sulfur (percentage level) was identified using EDX, 5–7% loss in Ni and 1–2% gain in sulfur as indicated by XPS
Dong *et al.*[153,154]	Ni-YSZ	Raman, SEM, XRD	727	100	*Ex situ*	After exposure for 120 h, the sample cooled with the furnace in the fuel with 100 ppm H_2S	Bulk nickel sulfide phases identified using Raman spectroscopy and XRD and morphology associated with melted particles identified using SEM
Cheng *et al.*[56,152]	Ni-YSZ	SEM/EDX, XRD, Raman	800	100	*Ex situ*	After exposure for 2–48 h, the sample cooled in the fuel with 100 ppm H_2S	Ni_3S_2, NiS, Ni_3S_4 identified by Raman spectroscopy, dramatic morphology change on Ni
		Raman	200–570	100	*In situ*		No bulk nickel sulfide formation at ~500 °C and above; bulk sulfides (*e.g.*, Ni_3S_2) started to form at ~430 °C and *below* accompanied with dramatic morphology changes
Ishikura *et al.*[58]	Ni-YSZ	SEM/EDX, Raman	900	5–20	*Ex situ*	Cell failed after sulfur poisoning, then sulfur was removed so that cell recovered partially	The significant sulfur presence was identified *via* EDX, local products appear melted
Lussier *et al.*[86]	Ni-YSZ	XAS, XPS	750	100–1500	*Ex situ*	Not clear	Ni chemical state of Ni, NiO, and nickel sulfide mixture, for failed sample, the insulating ring in center is depleted of Ni
Rasmussen and Hagen[85]	Ni-YSZ	SEM/EDX	850	2–100	*Ex situ*	Not clear	Short term exposure did not change nickel distribution, no nickel compounds found in post-test EDS
Li *et al.*[71,88]	Ni-YSZ	SEM/EDX, XRD	800	2000	*Ex situ*	After poisoning	Bulk nickel sulfides (NiS, Ni_4S_3) were detected
Zhang *et al.*[100]	Ni-YSZ and Ni-GDC	SEM/EDX	800	5–700	*Ex situ*	After poisoning and recovery, cooled with the furnace in N_2	No sulfur detected in EDX, significant morphology change on Ni as well as GDC but not on YSZ

sulfides (Ni_3S_2, NiS, Ni_3S_4, *etc.*) were identified on the sample surface accompanied with dramatic morphology changes. In contrast, if the sample, after exposure to the same H_2S gas mixture at elevated temperature, was *quenched* down (at a cooling rate of ~70 °C min^{-1} or faster) in the same fuel, *no* nickel sulfides could be detected.

This is expected from the bulk phase diagram for the Ni–H_2S–H_2 system. Taking the same example above, the equilibrium pH_2S/pH_2 concentration for Ni_3S_2 formation is ~4.7×10^{-3} or 4700 ppm at 800 °C, implying that bulk Ni_3S_2 will *not* form at 800 °C in a fuel with $pH_2S/pH_2 = 100$ ppm (note that other sulfides like NiS and Ni_3S_4 have even higher equilibrium pH_2S/pH_2 value). However, after exposure at 800 °C, when the sample is *cooled down slowly* (*e.g.*, ~3 °C min^{-1}) in the same fuel mixture ($pH_2S/pH_2 = 100$ ppm), the formation of Ni_3S_2 becomes energetically favorable when the temperature drops below ~420 °C because the equilibrium pH_2S/pH_2 for Ni_3S_2 to form drops by orders of magnitude as the temperature is lowered: it is only ~100 ppm at 420 °C, and further decreases rapidly to ~10 ppm at 323 °C, and ~0.3 ppm at 223 °C. The slow cooling makes sulfide formation possible when the reaction is thermodynamically favorable, which is accompanied by a dramatic morphology change.[56] In comparison, if the sample is quenched, although the bulk sulfidation reaction is still energetically favorable, the extent of reaction could be small in a short period of time, which explains the absence of bulk sulfides in the other studies. In addition, if the sample is cooled down in a slightly

reducing atmosphere or a *truly* inert atmosphere (*e.g.*, N_2 with pO_2 < ~10 ppm atm), extensive bulk sulfidation/oxidation may also be avoided.

It is advised that cooling the sample slowly in an "inert" atmosphere should be dealt with care because even the commercial ultra-high-purity (UHP) grade N_2 or Ar still contains oxygen content on the ~1 ppm level, and *small leaking from air* could easily cause the actual oxygen content to be orders of magnitude higher. When using UHP N_2 in the anode chamber and air on the cathode side, an open circuit voltage of ~0.06 to 0.07 V was recorded at 750 °C, corresponding to a pO_2 value of ~0.01 atm in the anode chamber. Therefore, when the anode chamber gas flow is switched from fuel gas to inert gas (*e.g.*, UHP N_2) and the sample cools down slowly, non-hermetic sealing makes the oxidation of Ni a clear possibility as the critical pO_2 for NiO formation is as low as $\sim 1 \times 10^{-16}$ atm at 1000 K and drops to $\sim 7 \times 10^{-27}$ atm at 700 K. We believe that this may also explain the surface roughening but the absence of sulfur on Ni surface in the study by Zhang *et al.* for samples exposed to 5–700 ppm H_2S at 800 °C and then recovered in H_2 and cooled in N_2.[100]

To date, only a few studies have successfully detected *adsorbed* sulfur species on the anode surface following sulfur poisoning using *ex situ* techniques.[53] Direct *in situ* identification of *adsorbed sulfur species* on a Ni-YSZ anode surface exposed in a fuel with ppm-level H_2S *at elevated temperatures* has *not* been successful.[56] The characterization of sulfur–anode interactions at the TPB appears to be even more challenging given the complexity of the reaction and many species involved (Ni, YSZ, H_2, H_2O, H_2S, and various adsorbed species and lattice defects like oxygen vacancies).

Finally, among various characterization techniques, Raman microspectroscopy is unique since it is highly sensitive to a wide range of *nickel sulfides* (*e.g*, Ni_3S_2, NiS, Ni_3S_4, and NiS_2) with good *spatial resolution down to ~1 μm*.[56,62,152] As mentioned above, Raman spectroscopy can also be conveniently configured for *in situ* characterization and provides valuable information from monitoring sulfide phase formation and phase transformation at elevated temperatures in different atmospheres to probing and mapping species or reaction intermediates adsorbed on electrode surfaces. Fig. 10 shows the optical micrographs collected during the *in situ* Raman microspectroscopy experiment of a same region on the polished surface of a dense Ni-YSZ cermet before and after the formation of nickel sulfide during exposure to a fuel of 100 ppm H_2S/H_2 at 440 °C. Shown in Fig. 11 are the corresponding Raman spectra obtained from the Ni region of the sample under the same conditions. The characteristic peaks in the Raman spectrum (collected after sulfide formation) correspond to those for Ni_3S_2 predicted from DFT-based calculations[155] (also see Section 5.3). This measurement suggests that Raman spectroscopy can be used to probe the formation of nickel sulfides under *in situ* conditions; it also implies that Raman spectroscopy may be used to validate predictions from DFT calculations. The combination of theoretical calculations and *in situ* Raman spectroscopy may provide valuable information vital to unraveling the mechanism of the interactions between H_2S and the Ni-YSZ cermet under various conditions. This can be applied to the study of corrosion of nickel-bearing alloys in sulfur-containing atmospheres at high temperatures.

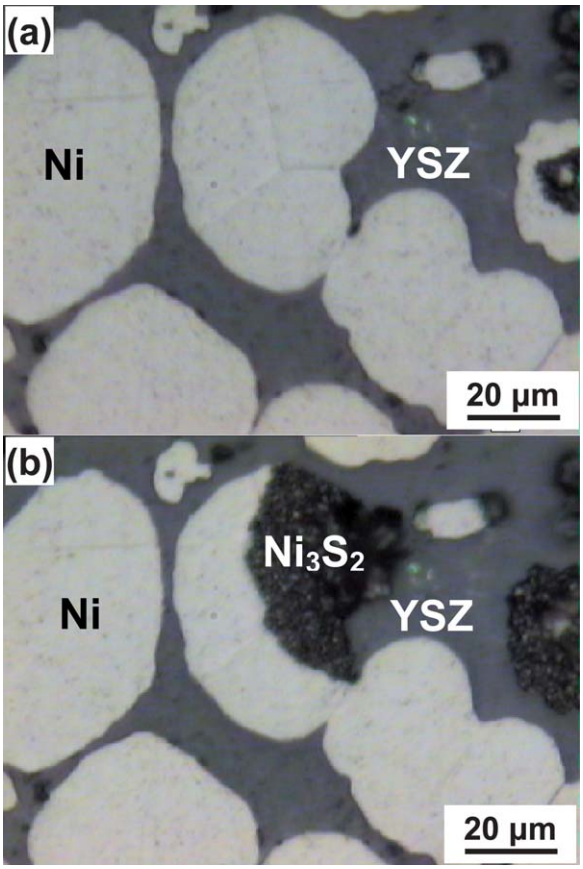

Fig. 10 Optical microscopy images during *in situ* Raman microspectroscopy characterization of a same region on the polished surface of a dense Ni-YSZ cermet before (a) and after (b) the formation of the bulk Ni_3S_2 phase when the cermet was exposed to a fuel of 100 ppm H_2S/H_2 at ~440 °C for 12 h[152] (Reprinted with permission from *J. Phys. Chem. C*, **111**, 17997. Copyright (2007) American Chemical Society).

4.2.2. Alternative anodes. The microstructural and chemical studies on the interactions between sulfur and alternative anode materials are rather limited. In particular, $Gd_2Ti_{1.4}Mo_{0.6}O_7$ (GTMO) has been shown to display higher power output in 10% H_2S/90% H_2 than in pure H_2.[122] Although no bulk sulfide phase was identified from the GTMO powder after exposure to 10% H_2S/90% H_2 for 5 days at 950 °C using XRD, the presence of Raman peaks corresponding to MoS_2 was identified on the surface of the GTMO anode after H_2S exposure, indicating that transition of the material's surface from an oxide phase to a thin sulfide phase might occur that contributes to the enhanced electrochemical performance as described before.[62] However, the explanation still needs to be verified by further studies. Synchrotron-based XRD and XAS would be ideally suited for probing the crystal structure, local atomistic arrangement, and electronic structure of conductive oxide electrodes under *in situ* conditions for fuel cell applications.

5 Understanding H_2S–anode interaction mechanism using DFT-based calculations

With continuing advances in the development of algorithms and rapid reduction in CPU costs, computational chemistry[156] plays

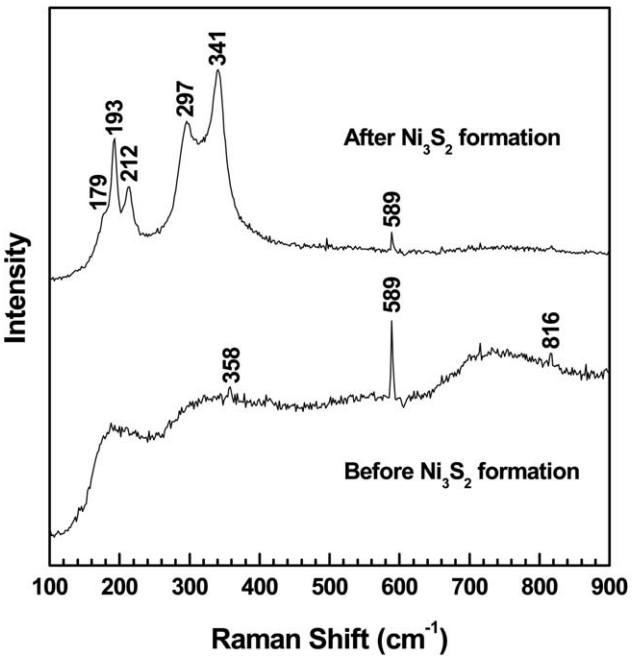

Fig. 11 Raman spectra taken *in situ* from the Ni region at 440 °C in a fuel of 100 ppm H_2S/H_2 before and after the formation of the bulk phase Ni_3S_2, as shown in Fig. 10[152] (Reprinted with permission from *J. Phys. Chem. C*, **111**, 17997. Copyright (2007) American Chemical Society).

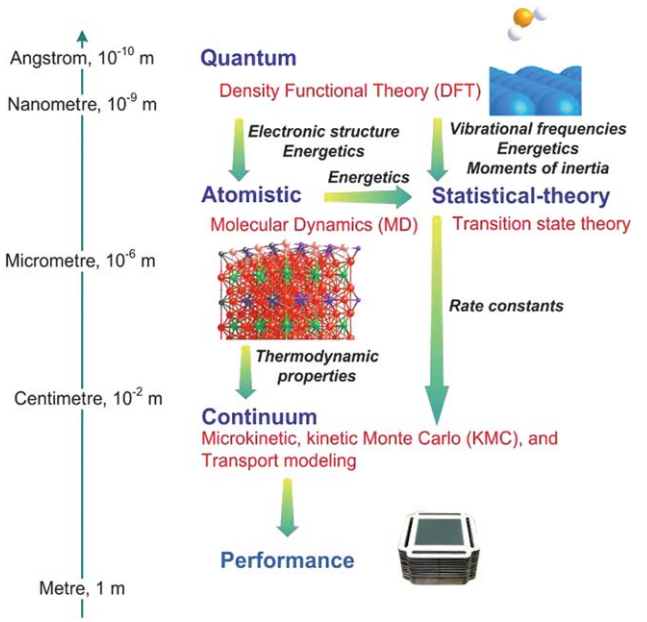

Fig. 12 Computational methods at different levels to design sulfur-tolerant SOFC anode materials.

a more and more important role in materials research.[157–159] For rational design of SOFC electrode materials, first-principle-based calculations employing different modeling techniques[160–162] have provided useful information that may not be readily obtained from experimental measurements. Among different computational techniques, DFT calculation is an effective approach for prediction of fundamental properties of materials and has offered important insights into sequences, mechanisms, and kinetics of electrode reactions on different crystallographic surfaces, with or without surface or bulk defects. This information is imperative to gaining a deeper understanding of the mechanism of elementary processes on the surfaces of SOFC electrodes.

While the conventional thermodynamics provides some useful insight into bulk phase stability[163] it is inadequate for the processes occurring on electrode surfaces and interfaces relevant to sulfur poisoning. Applications of advanced computational tools, as illustrated in Fig. 12,[160] can effectively guide us to rationally design sulfur-tolerant SOFC materials over a wide range of scales, from molecular to macroscopic levels.

In this section, we will first review the study of Ni and H_2S interactions using DFT-based calculations and the application of the same technique to exploring the sulfur tolerance of various alternative anode materials.[66,164,165] Then we will consider the effects of temperature and pressure (using *ab initio* atomistic thermodynamics) in order to gain an in-depth understanding of the sulfur poisoning processes under ordinary SOFC operating conditions. These computations, along with the experimental observations discussed earlier, provided direct evidence to support the hypothesis that sulfur poisoning of a conventional Ni-YSZ anode exposed to low ppm H_2S at elevated temperatures is due to adsorption of elemental sulfur on the Ni surface, not due to formation of nickel sulfide(s) as previously thought. They also helped us to understand many of the experimental observations presented in Sections 2, 3, 4, and 6. Finally, computational analysis of vibrational modes of surface species or new phases will be presented, which forms the scientific basis for peak assignment and for identification of reaction intermediates in spectroscopic experiments described in Section 4.

5.1. Understanding the sulfur-poisoning behavior in experiments

5.1.1. Reaction sequence and energetics for H_2S–anode interactions. Fig. 13 illustrates the interaction between H_2S and the Ni-YSZ anode at the macroscopic and molecular levels near the TPB (*i.e.*, H_2S-Ni-YSZ). To save computational time, the study was usually simplified as H_2S interaction with a metallic anode surface or an electrolyte surface at the two-phase boundary (2PB) (*i.e.*, H_2S-Ni or H_2S-YSZ). Earlier theoretical studies[66,164] pointed out that sulfur poisoning observed in low concentration H_2S at elevated temperatures is originated from the dissociation of sulfur-containing species and the adsorption of atomic sulfur (designated as S* here) on the anode surface.

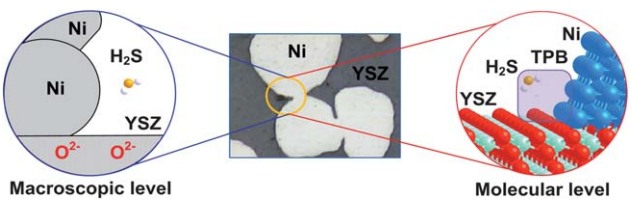

Fig. 13 The interaction between H_2S and Ni-YSZ cermet anodes at the macroscopic and molecular levels.

The strongly adsorbed S* species block active sites on the anode surface and thus increase the resistance to electrochemical oxidation of the fuel. In particular, Fig. 14 illustrates how a Ni-based anode surface can be constructed as an infinite slab with a proper vacuum space (~15 Å) (Fig. 14(a)) using periodic DFT calculations, while having four types of active sites (*i.e.*, atop, bridge, and three-fold fcc- and hcp-hollow sites) (Fig. 14(b)). As schematically illustrated in Fig. 14(c), the mechanism of S* formation can be ascribed as an interfacial reaction of adsorbed H_2S* with the Ni surface *via* two elementary steps of S–H bond cleavages (*i.e.*, $H_2S^* \rightarrow HS^* + H^*$ and $HS^* \rightarrow H^* + S^*$).

In addition, dissociative adsorption of H_2S on other metals (Fe, Pt, Pd, and Rh),[164–171] Ni–Cu alloys,[172] and oxides such as CeO_2 was also examined.[173,174] The associated energetic parameters (*i.e.*, reaction energies (ΔE) and reaction barriers (E_a)) for the interaction between H_2S and those materials have been obtained by DFT calculations, as summarized in Table 5.

Apart from ΔE and E_a for the individual reaction steps, another important parameter that can be obtained from DFT calculations is the adsorption energies (E_{ads}) of adspecies. E_{ads} is closely related to ΔE: higher exothermicity of an adsorption process is related to a *smaller* E_{ads} *of the reactant* and a *greater* E_{ads} *of the product*, as detailed in a previous work.[175] Table 6 summarizes calculated values for E_{ads} of reactants, intermediates, and products from H_2S interactions on selected metal and oxide surfaces.[66,166,168–171] S* is strongly bound to the surfaces (E_{ads} in the range of 5.14–6.60 eV), while HS* is less strongly bound (E_{ads} in the range of 1.36–3.80 eV). H_2S* is even more weakly bound (E_{ads} in the range of 0.09–1.20 eV) than S* and HS* with values being less than half that of HS*. The result also shows that E_{ads}'s of H* are ranged from 2.70 to 3.20 eV. Thus, the high exothermicities of the two elementary steps of H_2S dissociative adsorption on the surface are attributable to the stronger adsorption energies of the products (H* + HS* and H* + S*) and the relatively weak adsorption energies of the reactants (H_2S* and HS*, respectively). E_{ads} is also related to E_a: a strong adsorption, which is related to a high charge density distributed between a surface and an adsorbate, results in a lower charge density and weaker intra-molecular bonds within the adsorbate and, thus, reduces the dissociation barrier.[175] Since the adsorption reaction, $H_2S_{(g)} \rightarrow S^* + 2H^*$, involves only the S–H bond breaking steps, the lower E_a in Table 5 can be attributed to the stronger adsorptions of HS*, S*, and H*.

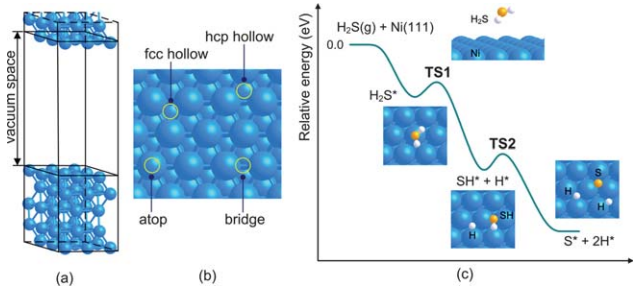

Fig. 14 (a) Schematic representation of a slab model with a proper vacuum space for periodic DFT calculations. (b) Four active sites on a (111) plane. (c) Schematic energy profile of gas-phase H_2S dissociation on Ni(111) forming atomic S* and H*. "*" denotes surface species. TS1 and TS2 are the transition states.

Table 5 Activation barriers (E_a) and reaction energies (ΔE) in the units of eV for the two elementary steps of $H_2S^* \rightarrow HS^* + H^*$ and $HS^* \rightarrow H^* + S^*$ in a H_2S dissociative adsorption process

	$H_2S^* \rightarrow HS^* + H^*$		$HS^* \rightarrow H^* + S^*$	
	E_a	ΔE	E_a	ΔE
Pt(111)[166]	0.02	−0.90	0.04	−1.19
Pd(111)[168]	0.37	−1.25	0.04	−0.73
Rh(211)[169]	0.01	−1.50	0.32	−1.50
Fe(100)[170]	0.25	−1.30	0.28	−1.30
Fe(110)[171]	0.10	−1.50	0.11	−1.35
Ni(100)[66]	0.29	−1.56	0.45	−1.05
Ni(111)[66]	0.15	−0.98	0.11	−0.86
CeO_2(111)[174]	0.08	−0.13	0.36	−1.08

Table 6 Adsorption energies (E_{ads}) of H_2S*, HS*, S*, and H* in the units of eV

	H_2S^*	HS*	S*	H*
Pt(111)[166]	0.90	3.00	5.14	—
Pd(111)[168]	0.71	3.02	5.15	—
Rh(211)[169]	1.00	3.69	6.00	2.86
Fe(100)[170]	0.50	3.60	6.00	2.70
Fe(110)[171]	1.20	3.80	5.80	3.20
Ni(100)[66]	0.83	3.72	5.96	2.84
Ni(111)[66]	0.67	2.95	5.14	2.91
CeO_2(111)[174]	0.09–0.15	1.36–1.46	6.60	—

The above calculations clearly suggest that elemental sulfur strongly adsorbs on Ni surfaces with a large exothermic ΔE and a small barrier E_a. The adsorbed sulfur blocks the access of hydrogen to active reaction sites (*e.g.*, TPBs), leading to a large drop in electrochemical activity, as described earlier in Section 2.2. The calculations also suggest that the adsorbed sulfur species exist primarily in the form of atomic sulfur instead of molecular H_2S. The large exothermic ΔE and very small E_a further imply fast kinetics for sulfur adsorption and sluggish kinetics for sulfur removal, consistent with the experimental observation of the instant drop in performance upon exposure to H_2S and a very slow recovery in performance after clean hydrogen is switched back, as described earlier. In addition, the similarity in ΔE and E_a for many alternative metals (*e.g.*, Pt and Fe) explains why replacing Ni with *these* metals does not solve the problems of sulfur poisoning, which is also consistent with experimental observations as described in Section 3.3.

5.1.2. Physical and chemical effects on sulfur adsorption. Furthermore, we can analyze adsorption energies based on the intrinsic effect of surface morphology and electronic structures that are related, respectively, to the physical and chemical properties of materials. According to the adsorption-energy calculations of S* on Pt(111),[166] Ni(111),[66,172,176] and Cu(111),[172] the strength of sulfur–metal bonds normally follows this order: three-fold-coordinated E_{ads} (fcc and hcp sites) > two-fold-coordinated E_{ads} (bridge sites) > one-fold-coordinated E_{ads} (atop sites), as shown in Table 7. In addition, sulfur adsorption is stronger on surface defects like steps, kinks, or terraces with higher coordination numbers than those on the corresponding

Table 7 E_{ads} of S* on Pt(111), Pd(111), Ni(111), and Cu(111) surfaces in the units of eV

	Pt(111)[166]	Pd(111)[168]	Ni(111)[66,172,176]	Cu(111)[172]
FCC	5.14	5.15	5.44, 5.16, 5.14	4.36
HCP	4.97		5.42, 5.06	4.32
Bridge	4.47		5.21, 5.02	4.21
Atop	3.04		3.92, 3.62, 3.62	3.22

perfect surfaces. Based on the results, we conclude that the higher the coordination of an adsorption site, the stronger its sulfur adsorption energy. Such *physical effect* (or coordination effect) from the surface geometric configuration is independent of materials.[177,178] Nevertheless, the results indicate that sulfur poisoning is *not* expected to be alleviated by changing physical features like surface morphology or grain orientations of metal catalysts in the anode.

On the other hand, the *chemical effect* of a certain adsorption process depends on materials, which is examined using density of states (DOS) analyses, as detailed in the d-band theory.[177,178] For example, Fig. 15(a) shows a DOS comparison of S* on Ni (111) and Cu(111) surfaces. The antibonding state of S* on Ni (111) with a higher energy relative to the Fermi level results in stronger adsorption, meaning that it is harder to excite electrons to the antibonding state with higher energy above the Fermi level for bond cleavage. In addition, the energy of the antibonding state corresponds to the DOS of metal surfaces. A downward shifted antibonding state relative to the Fermi level corresponds to the downward shifted and broader DOS of metals, as schematically illustrated in Fig. 15(b). Accordingly, the DOS of a metal with low energy and a broad distribution such as Cu(111) leads to a low antibonding state and weaker sulfur adsorption. The E_{ads} prediction from the DOS analysis agrees well with the experimental observation[65] that the adsorption enthalpy of S* on Ni surfaces is twice that on Cu surfaces, suggesting that Cu-based anodes would have much better tolerance to sulfur than Ni-based anodes for SOFCs, which is consistent with the experimental observation discussed in Section 3.3.

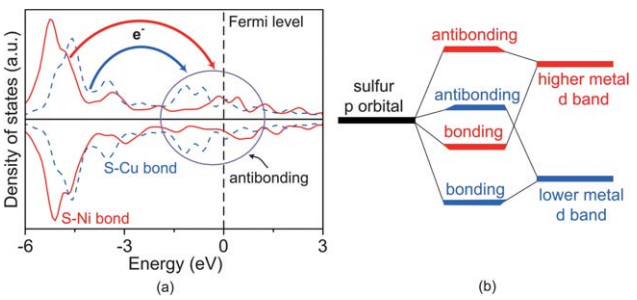

Fig. 15 (a) DOS analysis of S* on Ni(111) and Cu(111) in red and blue curves, respectively. A circle represents the antibonding states around the Fermi level. (b) A scheme of the energies of bonding and antibonding states corresponded to those of metal d bands.

5.1.3. Sulfur poisoning and approaches to achieve improved sulfur tolerance

•*Alternative metals and Ni–M alloys.* Based on the above analyses, the problem of sulfur poisoning for the Ni-YSZ anode can be attributed to the strong sulfur adsorption that blocks surface active sites, reduces the catalytic activity of neighboring sites, and results in the highly exothermic and low-barrier poisoning reaction. Therefore, minimizing the bond strength of S* by adjusting the DOS of metallic or alloy anodes seems *one* logical approach to enhancing sulfur tolerance, and the design rule for sulfur-tolerant anodes corresponds to the searching for a metal or alloy that has weak S* adsorption (low E_{ads}) with low-energy and broad-distribution DOS. As stated in Section 3.3, this is not trivial. Many common alternative metal catalysts such as Fe, Rh, and Pt have strong sulfur adsorption (see Section 5.1.1) and are expected to be poisoned readily. The studies that show promises are those focusing on completely replacing (*e.g.*, by Cu)[14,104,164,179] or partially introducing relatively inert metals or alloys (*e.g.*, Ni–Cu [172,180] and Ni–Sn [95,181] alloys) into anodes to weaken the interaction for S* and thus enhance their sulfur tolerance. However, a problem with these studies lies in the materials' inertness for sulfur adsorption, which usually also lowers their catalytic activities towards H_2 fuel oxidation represented by hydrogen adsorption energies since the catalytic activities of materials towards the hydrogen oxidation reaction (HOR) and H_2S dissociative adsorption usually have similar trends,[177,178] indicating that cell performance is sacrificed to achieve sulfur tolerance.

In light of these limitations, theoretical studies on metal alloys have been carried out to find metal and alloy materials that do not compromise performance for sulfur tolerance. To construct a Ni-M alloy, one of the Ni atoms on the top-most layer was removed and replaced with three alloying metals such as 3d and 4d transition metals, as in (a) and (b) of Fig. 16. The defective structure may provide a more practical model than the perfect ones with one Ni and three transition metals. According to the comparison of Ni and Cu,[172] the initial adsorption of H_2S is correlated with sulfur tolerance, and weaker E_{ads} for S* corresponds to better sulfur tolerance. Thus to evaluate sulfur

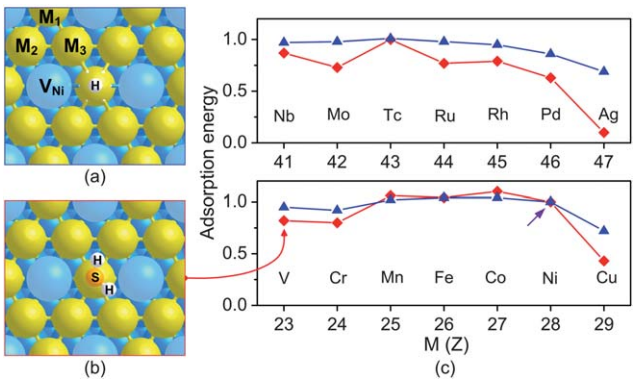

Fig. 16 Top views of (a) an adsorbed hydrogen and (b) an adsorbed H_2S on modified Ni(111) with various 3d and 4d metals (Ni-M). Solid gray balls (V_{Ni}) are Ni defects on the top-most layer. (c) Normalized adsorption energies relative to that on pure Ni(111) for H_2S* (red diamonds) and H_2* (blue triangles) on modified Ni(111) with various 3d and 4d transition metals.

tolerance of bimetallic Ni-M alloys, H_2S adsorption energies on various metals were calculated and normalized relative to that on pure Ni(111). As shown in Fig. 16(c), the comparative study demonstrates that metals like V, Cr, Cu, Mo, Ru, Rh, Pd, and Ag have significantly *lower* sulfur adsorption energy, E_{ads}, and their alloys with Ni are expected to be *more sulfur-tolerant* than pure Ni, while metals like Mn, Fe, Nb, and Tc have comparable E_{ads} and Co has slightly higher E_{ads} for sulfur adsorption, indicating comparable or even worse sulfur tolerance than Ni.

In addition to sulfur tolerance, a successful SOFC anode must also have high catalytic activity for fuel oxidation. Thus, we also calculated the dissociative adsorption energies of H_2 as a descriptor of catalytic activity for HOR following the method in the literature.[182] As displayed in Fig. 16(c), among the metals, Mo, Ru, and Rh have adsorption energy for H_2 (*i.e.*, catalytic activities) similar to Ni, while H_2 adsorption energy on Ag and Cu is much less indicating lower activity towards H_2 oxidation for those two metals.[14] These results highlight the promise of applying DFT calculations for screening sulfur-tolerant anode materials. They also suggest that, among the metals and alloys studied, Ni–Mo alloy seems to be a good candidate because it exhibits lower sulfur adsorption energy (better sulfur tolerance) than the pure Ni yet comparable hydrogen adsorption energy (good catalytic activity towards H_2 oxidation). This is confirmed by the experiment: as stated in Section 3.3, Ni-Mo-alloy based anodes showed improved sulfur tolerance over Ni-YSZ anodes.

•*Electrolyte modification.* Hypothetically, a second approach to enhance sulfur tolerance is to increase the activity of the electrolyte phase in the cermet anode for electrochemical oxidation of sulfur, as described by reaction (2) in Section 2. For the Ni-YSZ anode, S* on YSZ may be electrochemically oxidized to SO_2, and release electrons. However, this reaction could be kinetically slow in the middle of a YSZ region due to limited electronic conductivity of YSZ; it should be more active at or near the TPBs. The rate of the electrochemical oxidation of S* on the surface of the ceramic phase in a Ni-ceramic anode may increase with the ionic and electronic conductivities of the ceramic phase. This may explain (at least in part) why the substitution of YSZ by other ceramic phases (*e.g.*, GDC) showed different sulfur tolerances. Furthermore, when the oxygen conducting ceramic phase in the anode becomes more active in promoting the electrochemical oxidation of S* to SO_2 (thus removes S* on the surface of the ceramic phase), S* on the metal surface may migrate (spill over) to the clean TPB region (due to a concentration gradient) and get oxidized and removed there, as schematically illustrated in Fig. 17. Then the overall poisoning might then be alleviated.

The activity of the oxygen conducting ceramic phases, different from that of metallic Ni, depends on the formation energy of oxygen defects (vacancies) while the sulfur adsorption energy E_{ads} (S*) on the defects of most oxides seems to be similar (>6.50 eV). For example, the energies for forming defects in GDC, SSZ, and YSZ are 3.80, 5.80, and 7.80 eV, respectively, suggesting the activity of the electrolytes is in the order of GDC > SSZ > YSZ. On the experimental side, as stated in Section 3.2, cermet anodes like Ni-SSZ[53] and Ni-GDC[11,99,100] have been reported to have slightly better sulfur tolerance than Ni-YSZ (with less drop in power output as sulfur contaminants are introduced). However, the effect of the electrolyte phase on sulfur poisoning has not been carefully studied.

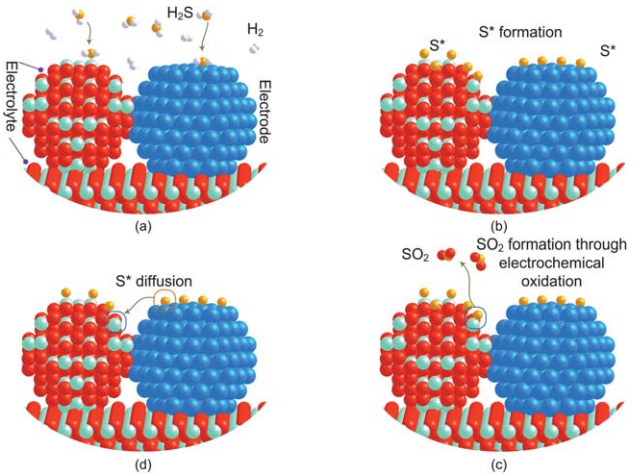

Fig. 17 Schematic illustration of S* formation and the removal from the oxidation reaction with oxygen ions (O^{2-}) from the electrolyte at the TPB. (a) Two grains of an electrolyte and an electrode are available with the gas-phase H_2S and H_2, impurity and fuel, respectively. (b) Two surfaces are saturated with S*. (c) S* on the TPB reacts with O^{2-} transported from the cathode *via* the electrochemical oxidation reaction, producing SO_2. (d) Accordingly, S* species on the high concentrated electrode grain diffuse to the low concentrated TPB.

In addition to oxygen ion conductors like YSZ, proton conductors such as $BaCeO_3$ are also considered. Table 8 compares energy for water dissociation and incorporation for proton ion $(HO)_{O^{\cdot}}$ (if applicable) formation on Ni, ZrO_2, CeO_2, and $BaCeO_3$. The results reveal that the energy for water adsorption and subsequent incorporation to $BaCeO_3$ and the formation of proton ions is significantly more favorable compared with those for ZrO_2 and CeO_2. How this will impact the sulfur tolerance and lead to the discovery of a new approach for improving anode sulfur tolerance are explained in Section 6.

5.2. *Ab initio* atomistic thermodynamics calculations: sulfur-tolerance under ordinary SOFC operating conditions

From the discussion above, DFT calculations have been applied to elucidate the mechanism for sulfur adsorption processes and related energetics for Ni as well as alternative metals, alloys, and oxides, and the energies for defects formation in electrolyte phases. However, DFT prediction is only valid *in vacuum at 0 K*. For practical purposes, external effects from the environment such as operational temperatures and pressures should be taken into consideration to make the calculation more relevant to practical operation. This is achieved by applying the thermodynamic correction to DFT results, as described in this section.

5.2.1. A modified Ni–S phase diagram that captures sulfur surface adsorption. Temperature and pressure effects can be taken into consideration in the DFT results by applying the thermodynamic correction (in Gibbs free energy calculation), *i.e.*, *ab initio* atomistic thermodynamics.[183,184] The DFT-computed energy (E^{DFT}) represents the Gibbs free energy at zero temperature in vacuum, or Helmholtz free energy ($F(T)$) at zero

Table 8 ΔE and E_a, in parentheses, in the units of eV of water dissociation on perfect and defective surfaces

	Ni(111)	ZrO_2(111)	CeO_2(111)	$BaCeO_3$(100)
Perfect surface				
$H_2O(g) \rightarrow H_2O^*$	−0.33	−0.41	−0.31	−0.71
$H_2O^* \rightarrow H^* + HO^*$	−0.11 (0.79)	−0.57 (0.51)	−0.06 (0.50)	−1.14 (0.11)
$HO^* \rightarrow H^* + O^*$	1.22 (1.45)	0.64 (0.40)	0.52 (0.71)	2.18 (0.39)
Defective surface				
$H_2O + V_{O^{\cdot\cdot}} \rightarrow (H_2O)_{O^{\cdot\cdot}}$		−0.82	−0.64	−0.58
$(H_2O)_{O^{\cdot\cdot}} + O_O^x \rightarrow 2(HO)_{O^{\cdot\cdot}}$		−0.32 (0.72)	−0.19 (0.71)	−1.29 (0.29)

temperature, $E^{DFT} = G(0, 0) = F(0)$. Specifically, the relation between Gibbs free energy and an internal energy from DFT calculations can be expressed as follows.

$$G(T, p) = G(0, 0) + G(0 \rightarrow T, 0 \rightarrow p^0) + G(T, p^0 \rightarrow p) = E^{DFT} + H(T, p^0) + RT\ln(p/p^0),$$

where E^{DFT} is directly computed from DFT, $H(T, p^0)$, which can be obtained from the thermodynamics database,[185] is the standard enthalpy contributing from rotations, vibrations, and entropy at $p^0 = 1$ atm, R is the ideal gas constant, and p/p^0 is a pressure-dependent function from the Maxwell relation. At a given pressure and temperature, the Gibbs free energy can be obtained by adding the last two terms of thermodynamic corrections to the DFT internal energy.

This method has successfully delineated the environmental effects on sulfur poisoning[66] and surface regeneration.[186] For example, Fig. 18 shows the *expanded* phase diagram from the theoretical prediction for the Ni–S system to explain the poisoning behavior on the Ni-based anode. This diagram represents the most stable phases with the lowest Gibbs free energy as a function of temperature and pressure (pH_2S/pH_2). Compared with the traditional Ni–S phase diagram that includes only bulk phases like Ni and nickel sulfides (*e.g.*, Ni_3S_2),[187,188] this new phase diagram also includes a transition region between those two phases that represent sulfur adsorption on the nickel surface when exposed to a trace amount of H_2S. The calculated phase diagram also agrees well with both experiments of sulfur adsorption on Ni catalysts[63] and anode poisoning for SOFCs.[27]

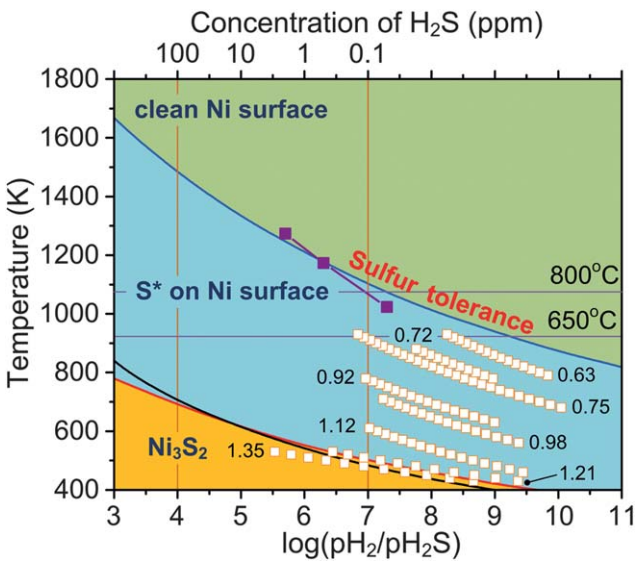

Fig. 18 S–Ni phase diagram calculated using *ab initio* atomistic thermodynamics. The three regions correspond to the phases of clean Ni, adsorbed sulfur S* on the nickel surface, and bulk Ni_3S_2. The experimental data are displayed in the black line, from Rosenqvist's bulk phase diagram,[188] the open squares, from the experimental result of S* with different area coverages,[63] and the purple squares, from the sulfur-tolerant experiment.[27]

The importance of this calculated Ni–S phase diagram is that it specifies the stability region for the *surface phase* of S* on Ni, which plays a key role in sulfur poisoning, and it makes up for the limitation of experimental techniques that are having difficulty in observing the adsorbed S* species under real SOFC operating conditions (see Section 4.2). Most sulfur poisoning behaviors for the Ni-YSZ cermet anode as described above in Sections 2 and 4 can be well explained from this modified Ni–S phase diagram. For example, the pH_2S/pH_2 concentration at which sulfur poisoning occurs is significantly lower than that for bulk Ni_3S_2 phase formation. In electrochemical characterizations, sulfur poisoning becomes more severe when the ratio of pH_2S/pH_2 increases or the temperature decreases, and this is due to increased sulfur surface coverage. Furthermore, the calculated diagram also helps predict sulfur tolerance or critical sulfur concentration beyond which sulfur poisoning will become significant, which corresponds to the boundary between clean Ni and S* phases (the blue curve) in the diagram. At typical planar SOFC operating temperatures of 650–800 °C, the critical pH_2S/pH_2 that avoids poisoning is in the range of 0.7–35.7 ppb, which is difficult and/or costly to reach in H_2 production. However, the diagram indicates that sulfur tolerance improves with increasing temperature: the required temperature for 1 ppm H_2S tolerance is ~950 °C, which is considered very high for SOFC operations, but is consistent with experimental observations.[27]

Sulfur tolerance could, in principle, be improved if the blue curve between clean Ni and S* on Ni surface could be lowered. According to Gibbs free energy calculations, this boundary corresponds to the three energetic parameters in the Ni–S system: E^{DFT}, $H(T, p^0)$, and $RT\ln(p/p^0)$ which then correspond to E_{ads}(S*), $H(H_2(g))$–$H(H_2S(g))$, and the partial pressure of sulfur contaminants (or pH_2S/pH_2), respectively. Since the latter two terms are related to the intrinsic properties of H_2S (g), they cannot be adjusted. Therefore, the tolerance line can be lowered by reducing E_{ads}(S*). Quantitatively, a drop of 0.1 eV (or 9.6 kJ mol^{-1}) of E_{ads}(S*) lowers the tolerance boundary by ~50 K. For example, E_{ads}(S*) on Cu(111) is about 1.3 eV (124.8 kJ mol^{-1}) less than that on Ni(111), hence, the tolerance boundary on Cu(111) would be lowered by ~650 K. This is consistent with the experimental observation, as detailed in Section 3.3: He *et al.*

observed that at 973 K, the Cu-based anode displays sulfur tolerance in fuels with a H_2S concentration of up to ~450 ppm.[104] In comparison, for the Ni-YSZ anode, to reach the sulfur tolerance of 500 ppm (log (pH_2/pH_2S) = 3.3) would correspond to a temperature of ~1650 K as in Fig. 18, which is almost exactly ~650 K higher than Cu.

5.2.2. Considerations for oxide materials. Another application of *ab initio* atomistic thermodynamics is for predicting the bulk phase stability of complex oxides in sulfur-containing fuels. For example, Fig. 19 plots the phase diagram of H_2S(g) interacting with proton conducting oxides of $BaCeO_3$ (BC, red line), $BaCe_{0.8}Y_{0.2}O_{3-\delta}$ (BCY, blue line), and $BaZr_{0.1}Ce_{0.7}Y_{0.2}O_{3-\delta}$ (BZCY, black line). The region below the phase boundary corresponds to the clean ABO_3-type oxide phase, while the region above the phase boundary corresponds to the situation when the ABO_3-type structure is disrupted by the formation of sulfides like BaS and binary oxides.[163,189] The results show that Zr doping dramatically stabilizes the oxide, and improves sulfur tolerance up to 100 ppm at 800 °C. It is comparable to the experimental result[1] wherein the Ni–$BaZr_{0.1}Ce_{0.7}Y_{0.2-x}Yb_xO_{3-\delta}$ anode sustained H_2S exposure for up to 20 ppm at 750 °C. The slight over-estimation of H_2S concentration compared to the experimental value might reflect the fact that Yb doping slightly increases the activity of the oxide, while sacrificing its stability. These computational results agree well with the description in Section 6 for the Ba$(Ce_{1-x}Zr_x)O_3$-based materials.

To improve the bulk stability of oxide anodes (*i.e.*, move up the boundary in the sulfide-oxide phase diagram in Fig. 19), the endothermicity of the transformation reaction from an oxide to a sulfide must be increased, *i.e.*, the oxide phase should be less likely to react with sulfur contaminants forming sulfides. On the other hand, the oxide phase may need to attract sulfur contaminants to reduce the S* presence on metallic anodes, suggesting that the oxide should be highly active. Similar to the behavior in the design of heterogeneous catalysts, these two criteria may yield a volcano-shaped curve in searching for the best sulfur-tolerant metal/oxide cermets. Specifically, the *catalytic activity* and *stability* of suitable oxides correspond to E_{ads}(S*) and ΔE of oxide to sulfide transformation, respectively. The high exothermicity of E_{ads}(S*) indicates that S* can quickly form oxides, while the high endothermicity of ΔE corresponds to better bulk phase stability of oxides. Thus, the wider the range between E_{ads}(S*) and ΔE is, the better is the sulfur tolerance of oxides.

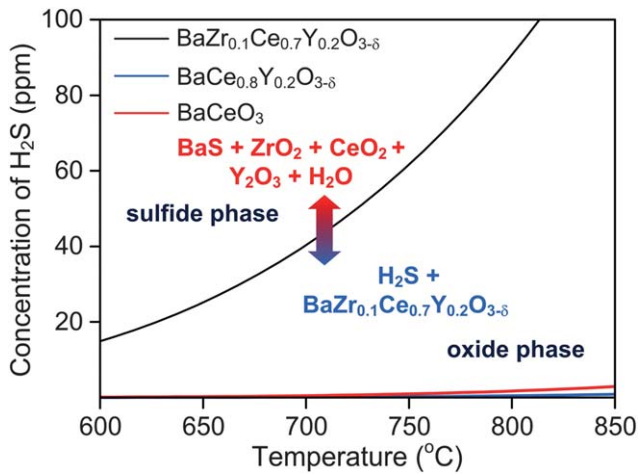

Fig. 19 Calculated sulfide-oxide phase diagram. The red, blue, and black lines correspond to the boundaries between oxides of $BaCeO_3$, $BaCe_{0.8}Y_{0.2}O_{3-\delta}$, and $BaZr_{0.1}Ce_{0.7}Y_{0.2}O_{3-\delta}$ and the corresponding sulfide phases, respectively, and can be represented as the sulfur tolerance of those three materials.

This range between E_{ads}(S*) and ΔE may be expanded further by incorporating the regeneration process of S* removal. This is plausible *via* adding a small amount of oxidants in the fuel to support the regeneration. However, aggressive oxidants like O_2 are likely to react with the H_2 fuel and form H_2O. This redox reaction cannot release electrons to the outside circuit and it will diminish the cell's performance. Another problem in the regeneration is the overdosing with oxidants that causes oxide formation on metallic anodes, which degrades the anode structure and electrochemical performance. Therefore, a mild oxidant such as H_2O is seen to be more feasible.[186] While the processes of poisoning and regeneration occur simultaneously on the anode, S* may be removed by the co-existing oxidant of water immediately after its formation. Although S* still can be formed on a surface, it requires a relatively high concentration of sulfur contaminants as the adsorbed water consumes part of them. We can consider this phenomenon as one wherein the E_{ads}(S*) is virtually reduced from the statistical viewpoint. Therefore, the boundary of clean Ni and S* in Fig. 18 is expected to pull down while that for oxide–sulfide in Fig. 19 is expected to move up so their sulfur tolerance can be improved. This constitutes one of the explanations why the sulfur tolerance can be dramatically enhanced by incorporating Ba$(Ce_{1-x}Zr_x)O_3$-based materials,[1] with high water activity, which is detailed in Section 6.

5.3. Vibrational mode analysis

DFT-based calculations have also been applied to classify the vibrational modes at the Γ point from the crystal symmetry and calculate the corresponding vibrational frequencies from optimized crystal structures. This information is vital to understanding the results of *in situ* and *ex situ* vibrational spectroscopy characterizations, which are powerful experimental tools for the study of sulfur–anode interactions. As detailed in Section 4.2.1, spectroscopic techniques like *in situ* Raman spectroscopy are sensitive to a wide range of reaction species including various bulk nickel sulfides under cell operational conditions. However, the corresponding spectra of these species may be hard to find in the available database. Such much-needed spectroscopic information can be obtained from DFT calculations: the computationally analyzed vibrations can assist for the peak assignment and phase identification from the experimentally acquired spectra to better understand the fundamentals of sulfur–anode interactions.

A successful example of this approach has been shown in the identification of Ni_3S_2, which is an important bulk phase in sulfur–anode interactions and observed from the *in situ* (as well as *ex situ*) Raman spectroscopy[56,152] (Section 4.1). This nickel-rich sulfide has not been clearly identified from previous

spectroscopic works.[190,191] On the other hand, our DFT calculation[155] clearly classifies that the crystal phonons have 6 Raman active modes, $2A_1 + 4E$ and helps identify the spectra obtained in our *in situ* sulfur-poisoning experiments.[56,62,152] In addition, spectroscopic information of other important products related to the irreversible sulfur poisoning, such as NiS, Ni_3S_4, and NiS_2, has also been extensively examined from the DFT calculations.[155] These results clarify the experimental observations[192–195] and provide valuable information to further understand sulfur–anode interactions.

6 Incorporation of $Ba(Ce_{1-x}Zr_x)O_3$-based materials in Ni-based cermet anode—a new approach to sulfur tolerance

It becomes clear from earlier discussions that most candidate sulfur-tolerant anode materials, which still exhibit some sensitivity even to low concentration (ppm level) of H_2S, have essentially the same reaction pathway: hydrogen combines with oxygen ion (from the electrolyte) at the triple phase boundary (TPB) to form water at the same geometrical location. This is the case not only for a Ni-YSZ cermet anode but also for the cermet anodes with Ni being replaced by other metals (*e.g.*, Cu) or YSZ being replaced by other oxygen ion conductors (*e.g.*, GDC). The situation remains similar when the whole Ni-YSZ anode is replaced by an electronically conducting oxide (*e.g.*, LST for up to 26 ppm H_2S or SMMO for 5 ppm). However, the active reaction sites may broaden to zones near the TPB as the oxygen ion conductivity of the conducting metal oxide increases; the wider the reaction zone the higher the oxygen ion conductivity. The presence of adsorbed sulfur on anode surface would not only block the adsorption and transport of hydrogen on the nickel surface but also impede the formation and evolution of water molecules from the active sites.[102] Sulfur tolerance is achieved probably through reduced adsorption of sulfur on anode surfaces, especially the metal surface for cermet anodes (*e.g.*, Cu in Cu-ceria-YSZ anode) or the oxide surface for the anodes based on LST or SMMO.

Recently, a very different approach was adopted to achieve better sulfur tolerance: replacing the oxygen ion conductor YSZ in a Ni-YSZ cermet anode by a mixed ion conductor like $BaZr_{0.1}Ce_{0.7}Y_{0.2-x}Yb_xO_3$ (BZCYYb),[1] which allows transport of both proton and oxygen vacancy (or ion). This Ni-BZCYYb cermet anode showed superior sulfur tolerance at 750 °C for up to ~20 ppm using a cell based on a BZCYYb electrolyte and up to ~50 ppm using a cell based on samaria doped ceria (SDC) electrolyte. The high performance suggests that the nickel metal in the cermet anode functions as the catalyst and the primary electronic conductor, such high critical pH_2S/pH_2 value is *two to three orders of magnitude higher* than that for a conventional Ni-YSZ cermet anode under similar conditions.[27] The displayed sulfur tolerance is also significantly better than the cermet anodes with YSZ replaced by other oxygen ion conductors of higher conductivity such as GDC and ScSZ,[53,100] as described earlier in Section 3.2.

It is also interesting to note that the cell impedance for the Ni-BZCYYb/SDC/LSCF cell shows sulfur poisoning (*i.e.*, increase in total cell interfacial resistance) under open circuit voltage conditions in *dry* H_2 (*i.e.*, without water vapor) but *not in humidified* H_2. While the detailed mechanism for the enhanced sulfur tolerance of the Ni-BZCYYb anode is yet to be determined, it is hypothesized that dissociative adsorption of water on the surface of BZCYYb facilitates the oxidation of the adsorbed sulfur or H_2S to SO_2 at or near the active sites. As evident from many experimental observations and as stated earlier in Section 5.1.3, water adsorption on the surfaces of $BaCeO_3$-based materials (*e.g.*, BZCY or BZCYYb) appears much more energetically favorable than on the surface of ZrO_2 or CeO_2-based materials. To date, however, it is still not clear how water vapor would facilitate sulfur oxidation on the anode surface under fuel cell conditions. One possibility is the oxidation of adsorbed sulfur (S*) through combination with adsorbed water (H_2O*) and lattice oxygen to form SO_2 and proton ions $(HO)_{\dot{o}}$:

$$S^* + 4O_o^x + 2H_2O^* = SO_{2(g)} + 4(HO)_{o^{\cdot}} + 4e^- \quad (16)$$

This reaction is expected to be slow due to the large number of electrons and reaction species involved. Another simpler hypothetical reaction pathway is the direct reaction between adsorbed water (or related species like dissociated OH) and adsorbed sulfur to form SO_2

$$S^* + 2H_2O^* = SO_{2(g)} + 2H_{2(g)} \quad (17)$$

As the surface coverage of S* can be relatively high (the S* is firmly adsorbed on the surface) while the concentration of SO_2 is relatively low (it readily desorbed from the surface), the probability for SO_2 and H_2 to react and form H_2S is relatively low. Finally, a third possibility is related to hydrogen incorporation into the BZCYYb phase, as schematically illustrated in Fig. 20. For the cell structure with Ni-BZCYYb anode and BZCYYb electrolyte, two anodic reaction pathways are at play. The first, designated as **R1** here, is the anodic process leading to water generation,

$$H_{2(g)} + O_O^x \rightarrow H_2O_{(g)} + V_{o^{\cdot\cdot}} + 2e'. \quad (18)$$

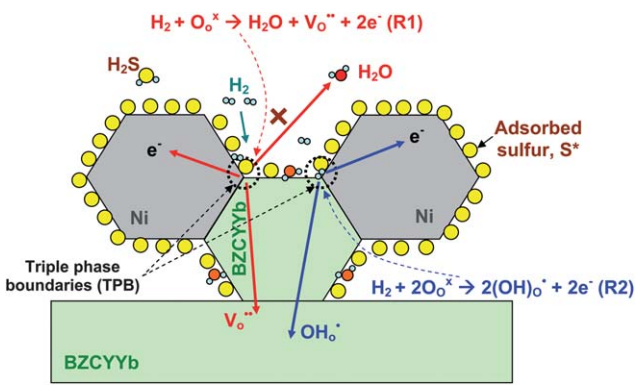

Fig. 20 Schematic showing the two anodic reaction pathways for the Ni-BZCYYb/BZCYYb anode structure under SOFC operating conditions. R1 represents the water generation reaction of $H_2 + O_O^x \rightarrow H_2O + V_{O^{\cdot\cdot}} + 2e'$, which is significantly hindered by the adsorbed sulfur on the electrode surface because of the large size of water molecule that has to be released from the TPB; R2 represents the hydrogen incorporation reaction of $H_2 + 2O_O^x \rightarrow 2(OH)_{O^{\cdot}} + 2e^-$, which may not be affected much by the adsorbed sulfur on the surface because of the small size of hydrogen that is incorporated into the lattice.

This reaction is identical to the dominating anodic reaction at the TPB for a Ni-YSZ cermet anode.[102] The second reaction pathway, designated as **R2** here, is the anodic process with hydrogen incorporation:

$$H_{2(g)} + 2O_{O}^{x} \rightarrow 2(OH)_{O^{\cdot}} + 2e^{-} \quad (19)$$

It is hypothesized that for the Ni-BZCYYb anode, water generation reaction **R1** may be slowed down significantly due to the geometrical blockage of adsorbed sulfur on the Ni surface and near the TPBs: because the water molecule has relatively large size, the blockage effect of adsorbed sulfur will be large. On the other hand, hydrogen incorporation reaction **R2** may *not* be impeded by the adsorbed sulfur because the size of hydrogen is very small; it might find its way to incorporate into the BZCYYb electrolyte near the TPB.

In contrast, reaction **R1** is the *only* possible pathway for a Ni-YSZ anode since YSZ does not have proton conductivity and, as a result, the sulfur poisoning will be much more significant compared with the Ni-BZCYYb anode. Further experimental and theoretical studies are needed to clarify the exact mechanism for enhanced sulfur tolerance.

It is noted that similar sulfur tolerance has been observed in the dense Ni–BZCY composite membrane for *hydrogen separation*. The hydrogen permeation flux remained stable at 900 °C when the H_2S concentration was 30 ppm.[196] Thus, Ni cermet anodes with BZCY-based materials may also have similar sulfur tolerance. As reported elsewhere,[1] a small amount of BaO spread to the surface of Ni grains in a Ni-BZCYYb cermet anode during processing at high temperatures may play a vital role in achieving the observed sulfur tolerance. In fact, when nano-sized BaO islands were created on the surface of the Ni grains in a Ni-YSZ cermet anode using a vapor phase deposition, the resistance to coking was dramatically enhanced.[2] The nanostructured BaO/Ni interfaces seem to be very efficient for the water-mediated carbon removal; they also showed good sulfur tolerance while maintaining high performance.

One limitation of BZCY or BZCYYb-based materials is the possible chemical reaction with H_2S. For example, BaS was formed when BZCY was exposed to H_2 with 60 ppm H_2S,[196] consistent with the prediction shown in Fig. 19. Indeed, the Ni-BZCYYb anode experienced rapid deterioration upon exposure to 100 ppm H_2S/H_2.[1] Finally, as discussed above, the sulfur tolerance of the BZCY or BZCYYb materials is associated with their ability to adsorb or absorb water. In addition, it is expected that increasing the Zr/Ce ratio may enhance the stability of the Ni-BZCY anode toward sulfur poisoning due to the reduced susceptibility towards reaction with H_2S.

7 Concluding remarks and future prospects

•Sulfur poisoning of Ni-YSZ anode

The detrimental effect of hydrogen sulfide in the fuel stream for SOFCs is well known and the sulfur poisoning behavior of Ni-YSZ anodes has been extensively studied. Under typical SOFC operating conditions (with *low* concentration of sulfur contaminants), H_2S quickly dissociates into hydrogen and elemental sulfur. It is the elemental sulfur that strongly adsorbs on the nickel surface and blocks the active sites for electrochemical oxidation of the fuel, leading to *increased* anode polarization or *sulfur poisoning effect*. This is supported by the experimental observation of an instant drop in fuel cell performance (or increase in anode polarization resistance) upon exposure of Ni-YSZ anodes to fuels containing H_2S of concentrations well below those predicted for bulk nickel sulfides formation. It is also corroborated by the absence of bulk nickel sulfides on Ni-YSZ anodes in *well-designed in situ* and *ex situ* experiments under similar conditions.

The degree or extent of sulfur poisoning is best described by the *change in exchange current density* or the *change in anode polarization resistance* (under open circuit conditions) upon exposure to H_2S because they are independent of bias conditions (*i.e.*, current density or cell voltage). The factors that critically influence the degree of sulfur poisoning are H_2S concentration (or the pH_2S/pH_2 ratio) and fuel cell operating temperature. Other factors that also influence the observed poisoning behavior include current density, cell voltage, the amount of nickel in the anode, test cell configuration, concentration of other gases (such as H_2O, CO_2, and CO), and the time of exposure, as revealed from various experiments and theoretical analysis.

The poisoning effect is reversible when the H_2S concentration is below the critical value for formation of bulk nickel sulfides. Within this limit, the *degradation* in performance (or the *change in anode polarization resistance*) can be completely recovered when H_2S is removed from the fuel, suggesting that the elemental sulfur on the Ni surface can be completely removed. It is noted, however, that the adsorption of sulfur on Ni is much faster than the removal of adsorbed sulfur (S*) from Ni surface. The rate of recovery (or sulfur removal) is faster at a higher operating temperature, in a lower H_2S concentration, and for a shorter period of exposure to H_2S. Once nickel sulfides are formed, however, it appears that the *degradation* in performance can no longer be completely recovered, even long after the removal of H_2S from the fuel, and even though the nickel sulfides may be completely converted back to nickel metal, suggesting that the formation of nickel sulfides may have an irreparable effect on anode performance. Further, other factors like contamination from other cell components (*e.g.*, sealant) and microstructural changes (due to coarsening of porous electrodes) may also induce irreversible effects on anode behavior.

•Alternative anode materials for sulfur tolerance

Various alternative anode materials and different combinations of them have been examined as sulfur-tolerant anodes for SOFCs. Among them, one prominent group is *nickel-free* conductive metal oxides, which are perceived to have the potential for solving the problems associated with Ni-based cermet anodes: susceptibility to poisoning by impurities like sulfur, destruction by re-oxidation, and deactivation by carbon deposition in hydrocarbon fuels. While many of them have showed excellent sulfur tolerance with electrolyte-supported cells, their applicability to practical high-performance cells is severely hindered by their low electrical conductivity, poor catalytic activity toward fuel oxidation, and limited compatibility with electrolyte (or other cell components) at high temperatures required for fabrication.

For anodes with Ni replaced by other metals, the main concern is poor performance due to low catalytic activity unless precious metals (*e.g.*, Pt and Pd) are introduced by infiltration. The use of precious metals, however, may not be economically feasible for practical applications. For most metal sulfide based anodes, the main concern is their instability in clean hydrogen fuel.

Ni-BZCYYb cermet anode is unique in the sense that Ni is still active as the catalyst for efficient hydrogen oxidation and as electronic conductor in the anode for current collection. Its excellent sulfur tolerance may be associated with the ability of the BZCYYb material for dissociative adsorption of water, which effectively promotes the removal of adsorbed sulfur from the TPB and enhances the sulfur tolerance. BaO nano-islands are also found on the surfaces of Ni that is co-fired with BZCYYb, which may further facilitate dissociative adsorption of water at the BaO/Ni interfaces and thus promote sulfur removal from the surface of Ni.[2]

Finally, it is worth mentioning that for all sulfur tolerant anode materials (except probably bulk metal sulfides), there usually appears to be a critical sulfur concentration above which the degradation in cell performance becomes significant.

•Achieving sulfur tolerance through surface modification

Although many new anode materials with better sulfur tolerance have been developed, the adoption of these materials in fuel cells is often hindered by their limited compatibility with other cell components (especially at high temperatures required for fabrication), inadequate catalytic activity toward fuel oxidation, and/or insufficient conductivity for current collection. Accordingly, surface modification of Ni-YSZ cermet anodes with proper catalytic coatings remains an attractive option for dramatic enhancement of tolerance to contaminants without compromising performance. It is proven that Ni-YSZ offers the highest performance in clean hydrogen among all materials ever studied for SOFC anodes in addition to its excellent compatibility with the YSZ electrolyte for cost-effective fabrication of anode-supported cells. The best approach is to minimize its sensitivity to sulfur using a very thin catalytic coating that does not significantly affect its activity for hydrogen oxidation and excellent electronic conductivity. In particular, modification of the Ni-YSZ cermet anode by incorporation of oxides *via* infiltration is a promising route to achieving sulfur tolerance while maintaining high performance. It is important to note, however, that the performance of the infiltrated Ni-YSZ anodes depends critically on the detailed microstructure, composition, morphology, and distribution/dispersion of the catalytic coating on the surface of Ni/YSZ.

•*Ex situ* and *in situ* characterizations

The interactions between sulfur compounds and anode materials for SOFCs have been characterized using various *ex situ* and *in situ* characterization techniques. *Ex situ* characterizations should be performed with great care to avoid complications introduced during sample preparation and transfer because samples may undergo undesirable changes when they are transferred from the actual testing conditions to the analysis chamber for characterization (due to changes in temperature and atmosphere). In contrast, *in situ* characterizations may be used to directly probe and map surface species or new phases on electrode surface under practical operating conditions, offering valuable information about electrode surface processes in real time. In particular, *in situ* Raman microspectroscopy is proven unique because it has demonstrated high sensitivity to various bulk and surface species and phases (including sulfides) relevant to sulfur poisoning with reasonable spatial resolution. It can be used to probe and map surface molecular processes or incipient new phase formation relevant to electrode kinetics under practical fuel cell operating conditions. It has been successfully applied to study the (bulk) sulfides formation and related phase transformations, providing valuable information about fundamental mechanisms for the sulfur–anode interactions in SOFCs. Further, when combined with simultaneous electrochemical measurements (*e.g.*, impedance spectroscopy), the surface species or phases identified using Raman spectroscopy can be directly correlated with electrochemical behavior and performance of the electrodes.

In addition, Raman measurements can also be used to validate DFT-based calculations. The vibrational mode frequencies can be calculated from the interaction forces between atoms when displacements are introduced. Comparison of the calculated frequencies with the measured ones from Raman spectroscopy enables the confirmation of the models used for DFT calculations.

•Theoretical calculations

While significant progress has been made in gaining insights into the mechanisms of the atomistic or molecular processes relevant to the interactions between H_2S and anode surfaces, major challenges still remain to bridge the gaps between models at different scales or between theoretical predictions and experiments.[197–203] One of the difficulties in application of DFT calculations to prediction of materials properties[200,203] is related to the errors from the delocalization of electron density and static correlation, especially for materials containing metal ions with open shell d or f electrons. This may affect the calculations of reaction sequence and adsorption energy, but can be corrected by introducing fractional charges or spins to the system.[200] In addition, DOS analysis of some oxides or sulfides with mixed electron distribution might produce fictitious band structures. This problem can be corrected using DFT + U theory with

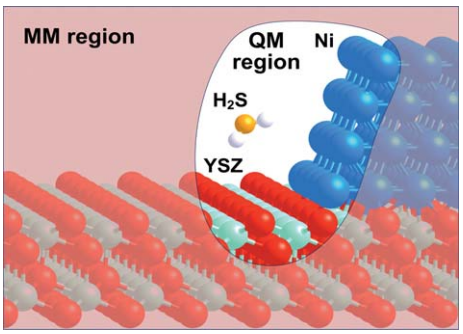

Fig. 21 Graphical illustration of the H_2S interaction with Ni/YSZ divided into two regions for applying the QM/MM (quantum mechanics/molecular mechanics) methodology.

suitable intra-atomic parameters of Coulomb and exchange energies.[203,204]

Furthermore, to assure practically useful results from DFT-based predictions, design factors for the highly complicated electrochemical systems must be examined. One possible way is to apply the quantum mechanics/molecular mechanics (QM/MM) methodology[205] to model practical sizes with the TPBs; it consists of two input regions, chemically active and non-active ones, treated by the QM and MM approaches, respectively. Fig. 21 schematically illustrates the TPB divided into the two regions. The most active part of the TPB can be modeled using high-accuracy quantum chemical calculations, while the vicinity can be treated with low-cost MM approaches. The QM/MM approach will allow modeling and simulation of larger-scale models over longer times. After clarifying the mechanisms of the H_2S interaction with anode surfaces at the TPB to design more sulfur-tolerant materials with high catalytic activity and durability, micro-kinetic modeling[206] or kinetic Monte Carlo (KMC)[207–209] simulations can be applied to explore the most probable reaction pathway. A prerequisite for making the most of kinetic simulations for these complex systems is to have a reliable prediction of the rate constant for each elementary step involved.[210,211]

Finally, an atomic force field approach may use parameters derived from DFT calculations and may be combined with molecular dynamics (MD) simulations to study the time-dependent evolution and temperature-dependent properties of anode systems. These atomistic simulations may also provide input phenomenological parameters needed for larger-scale continuum modeling for electrochemical measurements such as impedance spectroscopy. Considerable efforts are still required to develop proper continuum (phenomenological kinetics and transport) models to directly link the predictions from DFT/MD calculations with material performance, to validate model structures, and to estimate material parameters from macroscopic measurements (*e.g.*, catalytic and electrochemical properties). If successful, the *local* electrochemical response of an anode (governed by the thermodynamics and kinetics of the electrochemical reactions at the interfaces) may be linked to their *global* behavior by incorporating the effects of the nano- and microstructural geometry of the anode across length scales through a computational framework. These multi-scale modeling and simulation tools are imperative to achieving rational design of anode materials and structures with better sulfur tolerance and higher performance.

•Progress in desulfurization and anticipated sulfur content in typical fuels

Development in desulfurization of hydrocarbon fuels is important for SOFC research since most current SOFCs still use desulfurizer as a solution to sulfur poisoning. Recent progress in desulfurization is also very encouraging. For example, Toyota Motor Corporation and Aisin Seiki have announced successful demonstration of desulfurization unit capable of maintenance-free operation for up to 10 years.[212] Thus, a review of the state-of-the-art desulfurization technology and related materials would be very useful to researchers in the area of SOFC anode research. Another question is the anticipated level of H_2S that an SOFC anode should be able to tolerate. Realistically, it may be less practical to push the H_2S tolerance level far beyond tens of ppm[213–217] because today's clean natural gas for power generation usually contains sulfur of only up to ~30 ppm and sulfur concentration in diesel and gasoline also drops to the low ppm level. In addition, high sulfur concentration poses severe corrosion and environmental concerns; even if new anode materials can tolerate higher concentration of H_2S, the fuel cell exhaust containing sulfur compounds (SO_2, H_2S, *etc.*) still needs to be cleaned before being emitted to the air.

Acknowledgements

This material was based upon work supported as part of the HeteroFoaM Center, an Energy Frontier Research Center funded by the U.S. Department of Energy (DOE), Office of Science, Office of Basic Energy Sciences (BES) under Award Number DE-SC0001061. The authors would like to acknowledge the contributions of their past colleagues (Drs Shaowu Zha, Shizhong Wang, Jian Dong, Chendong Zuo, Songho Choi, and Mingfei Liu) to many experimental measurements and theoretical calculations summarized in this paper. ML acknowledges partial support from the WCU project at UNIST by the South Korean Government. JW, YC, and MCL acknowledge the use of computational resources from the National Center for High-Performance Computing, Taiwan, supported by INER.

References

1 L. Yang, S. Wang, K. Blinn, M. Liu, Z. Liu, Z. Cheng and M. Liu, *Science*, 2009, **326**, 126.
2 L. Yang, Y. Choi, W. Qin, H. Chen, K. Blinn, M. Liu, P. Liu, J. Bai, T. A. Tyson and M. Liu, *Nat. Commun.*, 2011, **2**, 357.
3 R. M. Ormerod, in *High Temperature Solid Oxide Fuel Cells: Fundamentals, Design and Applications*, ed. S. C. Singhal and K. Kendall, Elsevier Ltd, Oxford, UK, 2003, ch. 12, pp. 333–361.
4 Y. Yi, A. D. Rao, J. Brouwer and G. S. Samuelsen, *J. Power Sources*, 2005, **144**, 67–76.
5 A. Hawkes, I. Staffell, D. Brett and N. Brandon, *Energy Environ. Sci.*, 2009, **2**, 729–744.
6 J. Weissbart and R. Ruka, *J. Electrochem. Soc.*, 1962, **109**, 723–726.
7 A. L. Lee, R. F. Zabransky and W. J. Huber, *Ind. Eng. Chem. Res.*, 1990, **29**, 766–773.
8 A. L. Dicks, *J. Power Sources*, 1996, **61**, 113–124.
9 T. Suzuki, T. Yamaguchi, K. Hamamoto, Y. Fujishiro, M. Awano and N. Sammes, *Energy Environ. Sci.*, 2011, **4**, 940–943.
10 T. Kivisaari, P. Björnbom, C. Sylwan, B. Jacquinot, D. Jansen and A. de Groot, *Chem. Eng. J.*, 2004, **100**, 167–180.
11 J. P. Trembly, A. I. Marquez, T. R. Ohrn and D. J. Bayless, *J. Power Sources*, 2006, **158**, 263–273.
12 M. C. Williams, J. Strakey and W. Sudoval, *J. Power Sources*, 2006, **159**, 1241–1247.
13 T. M. Gür, M. Homel and A. V. Virkar, *J. Power Sources*, 2010, **195**, 1085–1090.
14 R. Singh, F. Guzman, R. Khatri and S. S. C. Chuang, *Energy Fuels*, 2010, **24**, 1176–1183.
15 J. Staniforth and K. Kendall, *J. Power Sources*, 1998, **71**, 275–277.
16 S. Baron, N. Brandon, A. Atkinson, B. Steele and R. Rudkin, *J. Power Sources*, 2004, **126**, 58–66.
17 P. Leone, A. Lanzini, M. Santarelli, M. Calì, F. Sagnelli, A. Boulanger, A. Scaletta and P. Zitella, *J. Power Sources*, 2010, **195**, 239–248.
18 R. J. F. van Gerwen, in *High Temperature Solid Oxide Fuel Cells: Fundamentals, Design and Applications*, ed. S. C. Singhal and K. Kendall, Elsevier Ltd, Oxford, UK, 2003, ch. 13, pp. 363–392.
19 T. Watanabe and S. Maeda, *Science and Technology Trends Quarterly Review*, 2007, pp. 65–78.

20 R.-U. Dietrich, J. Oelze, A. Lindermeir, C. Spitta, M. Steffen, T. Küster, S. Chen, C. Schlitzberger and R. Leithner, *J. Power Sources*, 2011, **196**, 7152–7160.
21 P. Nehter, J. B. Hansen and P. K. Larsen, *J. Power Sources*, 2011, **196**, 7347–7354.
22 M. Liu, P. V. Aravind, T. Woudstra, V. R. M. Cobas and A. H. M. Verkooijen, *J. Power Sources*, 2011, **196**, 7277–7289.
23 S. K. Park, J.-H. Ahn and T. S. Kim, *Appl. Energy*, 2011, **88**, 2976–2987.
24 D. J. Schroeder and P. Majumdar, *Int. J. Hydrogen Energy*, 2010, **35**, 11308–11314.
25 F. N. Cayan, M. Zhi, S. R. Pakalapati, I. Celik, N. Wu and R. Gemmen, *J. Power Sources*, 2008, **185**, 595–602.
26 C. Ding and T. Hashida, *Energy Environ. Sci.*, 2010, **3**, 1729–1731.
27 Y. Matsuzaki and I. Yasuda, *Solid State Ionics*, 2000, **132**, 261–269.
28 N. Q. Minh and T. Takahashi, *Science and Technology of Ceramic Fuel Cells*, Elsevier Science, Amsterdam, The Netherlands, 1995.
29 A. McEvoy, in *High Temperature Solid Oxide Fuels Cells: Fundamentals, Design and Applications*, ed. S. C. Singh and K. Kendall, Elsevier, Ltd, Oxford, UK, 2003, pp. 149–171.
30 W. Z. Zhu and S. C. Deevi, *Mater. Sci. Eng., A*, 2003, **362**, 228–239.
31 A. Atkinson, S. Barnett, R. J. Gorte, J. T. S. Irvine, A. J. McEvoy, M. Mogensen, S. C. Singhal and J. Vohs, *Nat. Mater.*, 2004, **3**, 17–27.
32 S. P. Jiang and S. H. Chan, *J. Mater. Sci.*, 2004, **39**, 4405–4439.
33 M. Gong, X. Liu, J. Trembly and C. Johnson, *J. Power Sources*, 2007, **168**, 289–298.
34 C. Sun and U. Stimming, *J. Power Sources*, 2007, **171**, 247–260.
35 Z. Cheng, J.-H. Wang and M. Liu, in *Solid Oxide Fuel Cells: Materials Properties and Performance*, ed. J. W. Fergus, R. Hui, X. Li, D. P. Wilkinson and J. Zhang, CRC Press, 2009, pp. 73–129.
36 S. McIntosh and R. J. Gorte, *Chem. Rev.*, 2004, **104**, 4845–4866.
37 D. Sarantaridis and A. Atkinson, *Fuel Cells*, 2007, **7**, 246–258.
38 A. Kuzjukevics and S. Linderoth, *Solid State Ionics*, 1997, **93**, 255–261.
39 J. Van herle, R. Ihringer and A. J. McEvoy, *ECS Trans.*, 1997, **97–40**, 565–574.
40 S. Majumdar, T. Claar and B. Flandermeyer, *J. Am. Ceram. Soc.*, 1986, **69**, 628–633.
41 A. C. Müller, D. Herbstritt and E. Ivers-Tiffée, *Solid State Ionics*, 2002, **152–153**, 537–542.
42 M. Radovic, E. Lara-Curzio, R. M. Trejo, H. Wang and W. D. Porter, *Ceramic Engineering and Science Proceedings*, 2008, 27-4, 79–85.
43 J. H. Yu, G. W. Park, S. Lee and S. K. Woo, *J. Power Sources*, 2007, **163**, 926–932.
44 T. Ishihara, N. M. Sammes and O. Yamamoto, in *High Temperature Solid Oxide Fuel Cells: Fundamentals, Design and Applications*, ed. S. C. Singhal and K. Kendall, Elsevier Ltd, Oxford, UK, 2003, ch. 4, pp. 83–117.
45 N. Q. Minh, *J. Am. Ceram. Soc.*, 1993, **76**, 563–588.
46 H. Koide, Y. Someya, T. Yoshida and T. Maruyama, *Solid State Ionics*, 2000, **132**, 253–260.
47 A. Glauche, T. Betz, S. Mosch, N. Trofimenko and M. Kusnezoff, *ECS Trans.*, 2009, **25**, 411–419.
48 S. Mukerjee, K. Haltiner, D. Klotzbach, J. Vordonis, A. Iyer, R. Kerr, V. Sprenkle, J. Y. Kim, K. Meinhardt, N. Canfield, J. Darsell, B. Kirby, T. K. Oh, G. Maupin, B. Voldrich and J. Bonnett, *ECS Trans.*, 2009, **25**, 59–63.
49 J. Pierre, *The Siemens Energy Coal Based SECA Program*, http://www.netl.doe.gov/publications/proceedings/10/seca/Presentations/Pierre_Presentation.pdf.
50 S. Primdahl and M. Mogensen, *J. Electrochem. Soc.*, 1997, **144**, 3409–3419.
51 I. Burmistrov and S. Bredikhin, *Ionics*, 2009, **15**, 465–468.
52 S. C. Singhal, R. J. Ruka, J. E. Bauerle, and C. J. Spengler, *Anode Development for Solid Oxide Fuel Cells, Final Technical Report*, 1986, The Department of Energy DOE/MC/22046-2371 (NITS Order No. DE87011136), Pittsburgh, PA.
53 K. Sasaki, K. Susuki, A. Iyoshi, M. Uchimura, N. Imamura, H. Kusaba, Y. Teraoka, H. Fuchino, K. Tsujimoto, Y. Uchida and N. Jingo, *J. Electrochem. Soc.*, 2006, **153**, A2023–A2029.
54 S. Zha, Z. Cheng and M. Liu, *J. Electrochem. Soc.*, 2007, **154**, B201–B206.
55 Z. Cheng, S. Zha and M. Liu, *J. Power Sources*, 2007, **172**, 688–693.
56 Z. Cheng and M. Liu, *Solid State Ionics*, 2007, **178**, 925–935.
57 V. Sprenkle, J. Y. Kim, K. Meinhardt, C. Lu, L. Chick, N. Canfield, J. Bonnett, S. Mukerjee and S. Shaffer, presented in part at the The 31st International Cocoa Beach Conference & Exposition on Advanced Ceramics and Composites, Daytona Beach, FL, 2007.
58 A. Ishikura, S. Sakuno, N. Komiyama, H. Sasatsu, N. Masuyama, H. Itoh and K. Yasumoto, *ECS Trans.*, 2007, **7**, 845–850.
59 J. B. Hansen, *Electrochem. Solid-State Lett.*, 2008, **11**, B178–B180.
60 J. B. Hansen and J. Rostrup-Nielsen, in *Handbook of Fuel Cells, Volumes 5 & 6: Advances in Electrocatalysis, Materials, Diagnostics and Durability*, ed. W. Vielstich, H. Yokokawa and H. A. Gasteiger, John Wiley & Sons, Ltd, 2009, vol. 6, ch. 65, pp. 1–13.
61 D. Waldbillig, D. G. Ivey and A. Wood, *Fuel Cell and Hydrogen Technologies, Proceedings of the International Symposium on Fuel Cell and Hydrogen Technologies*, 1st edn, 2005, pp. 237–249.
62 Z. Cheng, *Investigations into the Interactions between Sulfur and Anodes for Solid Oxide Fuel Cells*, http://hdl.handle.net/1853/22678.
63 J. G. McCarty and H. Wise, *J. Chem. Phys.*, 1980, **72**, 6332.
64 I. Alstrup, J. R. Rostrup-Nielsen and S. Røen, *Appl. Catal.*, 1981, **1**, 303–314.
65 C. H. Bartholomew, P. K. Agrawal and J. R. Katzer, *Adv. Catal.*, 1982, **31**, 135–242.
66 J.-H. Wang and M. Liu, *Electrochem. Commun.*, 2007, **9**, 2212–2217.
67 R. Barfod, A. Hagen, S. Ramousse, P. V. Hendriksen and M. Mogensen, *Fuel Cells*, 2006, **6**, 141–145.
68 S. Mukerjee, K. Haltiner, R. Kerr, L. Chick, V. Sprenkle, K. Meinhardt, C. Lu, J. Y. Kim and K. S. Weil, *ECS Trans.*, 2007, **7**, 59–65.
69 T. S. Li, H. Miao, T. Chen, W. G. Wang and C. Xu, *J. Electrochem. Soc.*, 2009, **156**, B1383–B1388.
70 P. Lohsoontorn, D. J. L. Brett and N. P. Brandon, *J. Power Sources*, 2008, **183**, 232–239.
71 T. S. Li and W. G. Wang, *J. Power Sources*, 2011, **196**, 2066–2069.
72 N. Lakshminarayanan and U. S. Ozkan, *Appl. Catal., A*, 2011, **393**, 138–145.
73 W. Feduska and A. O. Isenberg, *J. Power Sources*, 1983, **10**, 89–102.
74 J. F. B. Rasmussen and A. Hagen, *Fuel Cells*, 2010, **10**, 1135–1142.
75 S. Primdahl and M. Mogensen, *ECS Trans.*, 1999, **99–19**, 530–540.
76 E. Ivers-Tiffée and A. V. Virkar, in *High Temperature Solid Oxide Fuel Cells: Fundamentals, Design and Applications*, ed. S. C. Singhal and K. Kendall, Elsevier Ltd, Oxford, UK, 2003, ch. 9, pp. 229–260.
77 O. A. Marina, L. R. Pedersen and J. W. Stevenson, *Effect of sulfur and hydrocarbon fuels on titanate/ceria SOFC anodes*, http://www.netl.doe.gov/publications/proceedings/05/SECA_PeerReview/pdf/Marina.PNNL%20Fri%20AM.pdf.
78 N. U. Pujare, K. W. Semkow and A. F. Sammells, *J. Electrochem. Soc.*, 1987, **134**, 2639–2640.
79 DOE, DOE/MC/26355–92/C0062 (DE92040255), ed. N. J. Maskalick and E. R. Ray, Washington DC 1992.
80 E. Batawi, U. Weissen, A. Schuler, M. Keller and C. Voisard, *ECS Trans.*, 2001, **2001–16**, 140–147.
81 J. Iritani, K. Kougami, N. Komiyama, K. Nagata, K. Ikeda and K. Tomida, *ECS Trans.*, 2001, **2001–16**, 63–71.
82 L. Yang, Z. Cheng, M. Liu and L. Wilson, *Energy Environ. Sci.*, 2010, **3**, 1804–1809.
83 N. J. Maskalick, E. R. Ray and C. J. Spengler, in *Third Annual Fuel Cells Contractors Review Meeting*, ed. W. J. Huber, DOE, DOE/METC—91/6120 (DE 91002085), Washington, DC, 1992, pp. 116–108.
84 A. Hagen, J. F. B. Rasmussen and K. Thydén, *J. Power Sources*, 2011, **196**, 7271–7276.
85 J. F. B. Rasmussen and A. Hagen, *J. Power Sources*, 2009, **191**, 534–541.
86 A. Lussier, S. Sofie, J. Dvorak and Y. U. Idzerda, *Int. J. Hydrogen Energy*, 2008, **33**, 3945–3951.
87 S. J. Xia and V. I. Birss, *ECS Trans.*, 2005, **2005–07**, 1275–1283.
88 T. S. Li, W. G. Wang, T. Chen, H. Miao and C. Xu, *J. Power Sources*, 2010, **195**, 7025–7032.
89 H. Kurokawa, T. Z. Sholklapper, C. P. Jacobson, L. C. De Jonghe and S. J. Visco, *Electrochem. Solid-State Lett.*, 2007, **10**, B135–B138.
90 D. G. Ivey, E. Brightman and N. Brandon, *J. Power Sources*, 2010, **195**, 6301–6311.
91 J. W. Fergus, *Solid State Ionics*, 2006, **177**, 1529–1541.
92 J. W. Yun, S. P. Yoon, S. Park, H. S. Kim and S. W. Nam, *Int. J. Hydrogen Energy*, 2011, **36**, 787–796.

93 M. Smith and A. J. McEvoy, *ECS Trans.*, 2005, **2005–07**, 1437–1444.
94 M. J. Smith and A. J. McEvoy, *ECS Trans.*, 2007, **7**, 373–380.
95 O. A. Marina, C. A. Coyle, M. H. Engelhard and L. R. Pederson, *J. Electrochem. Soc.*, 2011, **158**, B424–B429.
96 J. C. Ruiz-Morales, D. Marrero-Lopez, M. Galvez-Sanchez, J. Canales-Vazquez, C. Savaniu and S. N. Savvin, *Energy Environ. Sci.*, 2010, **3**, 1670–1681.
97 M. R. Pillai, I. Kim, D. M. Bierschenk and S. A. Barnett, *J. Power Sources*, 2008, **185**, 1086–1093.
98 J. P. Ouweltjes, P. V. Aravind, N. Woudstra and G. Rietveld, *J. Fuel Cell Sci. Technol.*, 2006, **3**, 495–498.
99 P. V. Aravind, J. P. Ouweltjes, N. Woudstra and G. Rietveld, *Electrochem. Solid-State Lett.*, 2008, **11**, B24–B28.
100 L. Zhang, S. P. Jiang, H. Q. He, X. Chen, J. Ma and X. C. Song, *Int. J. Hydrogen Energy*, 2010, **35**, 12359–12368.
101 E. Brightman, D. G. Ivey, D. J. L. Brett and N. P. Brandon, *J. Power Sources*, 2011, **196**, 7182–7187.
102 W. G. Bessler, M. Vogler, H. Stormer, D. Gerthsen, A. Utz, A. Weber and E. Ivers-Tiffee, *Phys. Chem. Chem. Phys.*, 2010, **12**, 13888–13903.
103 T. J. Kirk and J. Winnick, *J. Electrochem. Soc.*, 1993, **140**, 3494–3496.
104 H. P. He, R. J. Gorte and J. M. Vohs, *Electrochem. Solid-State Lett.*, 2005, **8**, A279–A280.
105 L. Zhao, X. Ye and Z. Zhan, *J. Power Sources*, 2011, **196**, 6201–6204.
106 S. Choi, *Development of SOFC anodes resistant to sulfur poisoning and carbon deposition*, http://hdl.handle.net/1853/26601.
107 O. A. Marina, N. L. Canfield and J. W. Stevenson, *Solid State Ionics*, 2002, **149**, 21–28.
108 O. A. Marina and J. W. Stevenson, *Development of ceramic composites as SOFC anodes*, http://www.netl.doe.gov/publications/proceedings/03/seca-review/marina.pdf.
109 O. A. Marina, *Development of advanced SOFC anodes*, http://www.netl.doe.gov/publications/proceedings/04/seca-wrkshp/PNNL%20-%20Marina.pdf.
110 R. Mukundan, E. L. Brosha and F. H. Garzon, *Electrochem. Solid-State Lett.*, 2004, **7**, A5–A7.
111 H. Kurokawa, L. Yang, C. P. Jacobson, L. C. De Jonghe and S. J. Visco, *J. Power Sources*, 2007, **164**, 510–518.
112 A. Burke, S. Li, J. Winnick and M. Liu, *J. Electrochem. Soc.*, 2004, **151**, D55–D60.
113 L. Aguilar, S. W. Zha, S. W. Li, J. Winnick and M. Liu, *Electrochem. Solid-State Lett.*, 2004, **7**, A324–A326.
114 L. Aguilar, S. W. Zha, Z. Cheng, J. Winnick and M. L. Liu, *J. Power Sources*, 2004, **135**, 17–24.
115 Z. Cheng, S. W. Zha, L. Aguilar and M. L. Liu, *Solid State Ionics*, 2005, **176**, 1921–1928.
116 Z. Cheng, S. W. Zha, L. Aguilar, D. Wang, J. Winnick and M. L. Liu, *Electrochem. Solid-State Lett.*, 2006, **9**, A31–A33.
117 M. Cooper, K. Channa, R. De Silva and D. J. Bayless, *J. Electrochem. Soc.*, 2010, **157**, B1713–B1718.
118 N. Danilovic, J.-L. Luo, K. T. Chuang and A. R. Sanger, *J. Power Sources*, 2009, **192**, 247–257.
119 N. Danilovic, J.-L. Luo, K. T. Chuang and A. R. Sanger, *J. Power Sources*, 2009, **194**, 252–262.
120 S. W. Zha, P. Tsang, Z. Cheng and M. L. Liu, *J. Solid State Chem.*, 2005, **178**, 1844–1850.
121 S. W. Zha, Z. Cheng and M. L. Liu, *Electrochem. Solid-State Lett.*, 2005, **8**, A406–A408.
122 S. Zha, Z. Cheng and M. Liu, *ECS Trans.*, 2006, **1**, 293–302.
123 Y. H. Huang, R. I. Dass, Z. L. Xing and J. B. Goodenough, *Science*, 2006, **312**, 254–257.
124 Y. H. Huang, R. I. Dass, J. C. Denyszyn and J. B. Goodenough, *J. Electrochem. Soc.*, 2006, **153**, A1266–A1272.
125 G. Xiao, Q. Liu, X. Dong, K. Huang and F. Chen, *J. Power Sources*, 2010, **195**, 8071–8074.
126 X. C. Lu, J. H. Zhu, Z. Yang, G. Xia and J. W. Stevenson, *J. Power Sources*, 2009, **192**, 381–384.
127 S. Tao and J. T. S. Irvine, *J. Electrochem. Soc.*, 2004, **151**, A252–A259.
128 X. J. Chen, Q. L. Liu, S. H. Chan, N. P. Brandon and K. A. Khor, *J. Electrochem. Soc.*, 2007, **154**, B1206–B1210.
129 C. Peng, J. Luo, A. R. Sanger and K. T. Chuang, *Chem. Mater.*, 2009, **22**, 1032–1037.
130 S. Wang, M. Liu and J. Winnick, *J. Solid State Electrochem.*, 2001, **5**, 188–195.
131 R. Moos and K. H. Hardtl, *J. Appl. Phys.*, 1996, **80**, 393–400.
132 N. U. Pujare, K. J. Tsai and A. F. Sammells, *J. Electrochem. Soc.*, 1989, **136**, 3662–3678.
133 C. Yates and J. Winnick, *J. Electrochem. Soc.*, 1999, **146**, 2841–2844.
134 K. T. Chuang, A. R. Sanger, S. V. Slavov and J. C. Donini, *Int. J. Hydrogen Energy*, 2001, **26**, 103–108.
135 M. Liu, G. L. Wei, J. L. Luo, A. R. Sanger and K. T. Chuang, *J. Electrochem. Soc.*, 2003, **150**, A1025–A1029.
136 G. L. Wei, M. Liu, J. L. Luo, A. R. Sanger and K. T. Chuang, *J. Electrochem. Soc.*, 2003, **150**, A463–A469.
137 L. Zhong, M. Liu, G. L. Wei and K. Chuang, *Chin. J. Chem. Eng.*, 2003, **11**, 245–248.
138 J.-J. Chen, L. Zhong, G.-L. Wei and K. Chuang, *J. S. China Univ. Tech.*, 2004, **32**, 1–4.
139 G. L. Wei, J. L. Luo, A. R. Sanger and K. T. Chuang, *J. Electrochem. Soc.*, 2004, **151**, A232–A237.
140 L. Zhong, J. Chen, G. Wei, J. Luo and K. Chuang, *J. Chem. Ind. Eng.*, 2004, **55**, 1732–1735.
141 G. L. Wei, J. L. Luo, A. R. Sanger and K. T. Chuang, *J. New Mater. Electrochem. Syst.*, 2005, **8**, 59–64.
142 L. Zhong, G.-L. Wei, J.-L. Luo and K. Chuang, *Acta Scientiarum Natralium Universitatis Sunyatseni*, 2005, **44**, 61–65.
143 Z. Xu, J. Luo and K. T. Chuang, *J. Electrochem. Soc.*, 2007, **154**, B523–B527.
144 V. Vorontsov, J. L. Luo, A. R. Sanger and K. T. Chuang, *J. Power Sources*, 2008, **183**, 76–83.
145 K. T. Chuang, J. Luo and A. R. Sanger, *Chemical Industry and Chemical Engineering Quarterly*, 2008, **14**, 69–76.
146 Z.-R. Xu, J.-L. Luo and K. T. Chuang, *J. Power Sources*, 2009, **188**, 458–462.
147 V. Vorontsov, W. An, J. L. Luo, A. R. Sanger and K. T. Chuang, *J. Power Sources*, 2008, **179**, 9–16.
148 J. Winkler, P. V. Hendriksen, N. Bonanos and M. Mogensen, *J. Electrochem. Soc.*, 1998, **145**, 1184–1192.
149 S. B. Adler, *J. Electrochem. Soc.*, 2002, **149**, E166–E172.
150 D. W. Dees, U. Balachandran, S. E. Dorris, J. J. Heiberger, C. C. McPheeters and J. J. Picciolo, *ECS Trans.*, 1989, **89**(11), 317–321.
151 M. B. Pomfret, J. C. Owrutsky and R. A. Walker, *Annu. Rev. Anal. Chem.*, 2010, **3**, 151–174.
152 Z. Cheng, H. Abernathy and M. Liu, *J. Phys. Chem. C*, 2007, **111**, 17997–18000.
153 J. Dong, S. Zha and M. Liu, *ECS Trans.*, 2005, **2005–07**, 1284–1293.
154 J. Dong, Z. Cheng, S. W. Zha and M. L. Liu, *J. Power Sources*, 2006, **156**, 461–465.
155 J.-H. Wang, Z. Cheng, J.-L. Bredas and M. Liu, *J. Chem. Phys.*, 2007, **127**, 214705/214701–214705/214708.
156 F. Jensen, *Introduction to Computational Chemistry*, John Wiley & Sons Inc, New York, 1999.
157 J. H. Wang, Y. M. Choi and M. Liu, in *Quantum Chemical Calculations of Surfaces and Interfaces of Materials*, ed. V. A. Basiuk and P. Ugliengo, American Scientific Publishers, Los Angeles, 2008, ch. 14, pp. 289–304.
158 Y. Choi, D. Mebane, J.-H. Wang and M. Liu, *Top. Catal.*, 2007, **46**, 386–401.
159 Y. Choi, M. C. Lin and M. Liu, *J. Power Sources*, 2010, **195**, 1441–1445.
160 L. J. Broadbelt and R. Q. Snurr, *Appl. Catal., A*, 2000, **200**, 23–46.
161 M. Neurock, *J. Catal.*, 2003, **216**, 73–88.
162 J. Greeley, J. K. Nørskov and M. Mavrikakis, *Annu. Rev. Phys. Chem.*, 2002, **53**, 319–348.
163 Z. Cheng, S. W. Zha and M. L. Liu, *J. Electrochem. Soc.*, 2006, **153**, A1302–A1309.
164 Y. M. Choi, C. Compson, M. C. Lin and M. L. Liu, *Chem. Phys. Lett.*, 2006, **421**, 179–183.
165 N. M. Galea, E. S. Kadantsev and T. Ziegler, *J. Phys. Chem. C*, 2007, **111**, 14457–14468.
166 A. Michaelides and P. Hu, *J. Chem. Phys.*, 2001, **115**, 8570–8574.
167 D. R. Alfonso, *Surf. Sci.*, 2008, **602**, 2758–2768.
168 D. R. Alfonso, A. V. Cugini and D. C. Sorescu, *Catal. Today*, 2005, **99**, 315.
169 B. McAllister and P. Hu, *J. Chem. Phys.*, 2005, **122**, 84709.
170 D. E. Jiang and E. A. Carter, *J. Phys. Chem. B*, 2004, **108**, 19140–19145.
171 D. E. Jiang and E. A. Carter, *Surf. Sci.*, 2005, **583**, 60–68.

172 Y. M. Choi, C. Compson, M. C. Lin and M. Liu, *J. Alloys Compd.*, 2007, **427**, 25–29.
173 W.-F. Huang, H.-T. Chen and M. C. Lin, *J. Phys. Chem. C*, 2009, **113**, 20411–20420.
174 H.-T. Chen, Y. Choi, M. Liu and M. C. Lin, *J. Phys. Chem. C*, 2007, **111**, 11117.
175 S.-C. Huang, C.-H. Lin and J. H. Wang, *J. Phys. Chem. C*, 2010, **114**, 9826.
176 E. J. Albenze and A. Shamsi, *Surf. Sci.*, 2006, **600**, 3202–3216.
177 B. Hammer and J. K. Norskov, *Adv. Catal.*, 2000, **45**, 71.
178 J. K. Norskov, T. Bligaard, B. Hvolbak, F. Abild-Pedersen, I. Chorkendorff and C. H. Christensen, *Chem. Soc. Rev.*, 2008, **37**, 2163.
179 H. Kim, J. M. Vohs and R. J. Gorte, *Chem. Commun.*, 2001, 2334–2335.
180 C. M. Grgicak, M. M. Pakulska, J. S. O'Brien and J. B. Giorgi, *J. Power Sources*, 2008, **183**, 26.
181 J. A. Rodriguez, S. Chaturvedi, T. Jirsak and J. Hrbek, *J. Chem. Phys.*, 1998, **109**, 4052.
182 J. R. Kitchin, J. K. Norskov, M. A. Barteau and J. G. Chen, *J. Chem. Phys.*, 2004, **120**, 10240–10246.
183 W.-X. Li, C. Stampfl and M. Scheffler, *Phys. Rev. B: Condens. Matter*, 2003, **68**, 165412.
184 S. Laursen and S. Linic, *Phys. Rev. Lett.*, 2006, **97**, 026101.
185 NIST, http://webbook.nist.gov/.
186 J.-H. Wang and M. Liu, *J. Power Sources*, 2008, **176**, 23–30.
187 N. Barbouth and J. Oudar, *C. R. Acad. Sci. Paris, Ser. C*, 1969, **269**, 1618.
188 T. Rosenqvist, *J. Iron Steel Inst., London*, 1954, **176**, 37.
189 J. Li, J.-L. Luo, K. T. Chuang and A. R. Sanger, *Electrochim. Acta*, 2008, **53**, 3701–3707.
190 U. S. Ozkan, L. Zhang, S. Ni and E. Moctezuma, *Energy Fuels*, 1994, **8**, 830–838.
191 D. W. Bishop, P. S. Thomas and A. S. Ray, *Mater. Res. Bull.*, 2000, **35**, 1123–1128.
192 G. Shen, D. Chen, K. Tang, C. An, Q. Yang and Y. Qian, *J. Solid State Chem.*, 2003, **173**, 227–231.
193 C. de las Heras and F. Agulló-Rueda, *J. Phys.:Condens. Matter*, 2000, **12**, 5317.
194 E. Anastassakis and C. H. Perry, *J. Chem. Phys.*, 1976, **64**, 3604–3609.
195 T. Suzuki, K. Uchinokura, T. Sekine and E. Matsuura, *Solid State Commun.*, 1977, **23**, 847–852.
196 S. Fang, L. Bi, X. Wu, H. Gao, C. Chen and W. Liu, *J. Power Sources*, 2008, **183**, 126–132.
197 J. Fahrenkamp-Uppenbrink, P. Szuromi, J. Yeston and R. Coontz, *Science*, 2008, **321**, 783.
198 A. J. Stone, *Science*, 2008, **321**, 787–789.
199 D. C. Clary, *Science*, 2008, **321**, 789–791.
200 A. J. Cohen, P. Mori-Sánchez and W. Yang, *Science*, 2008, **321**, 792–794.
201 G.-J. Kroes, *Science*, 2008, **321**, 794–797.
202 M. L. Klein and W. Shinoda, *Science*, 2008, **321**, 798–800.
203 E. A. Carter, *Science*, 2008, **321**, 800–803.
204 A. I. Liechtenstein, V. I. Anisimov and J. Zaanen, *Phys. Rev. B: Condens. Matter*, 1995, **52**, R5467.
205 H. Lin and D. Truhlar, *Theor. Chem. Accounts: Theor. Comput. Model. Theor. Chim. Acta*, 2007, **117**, 185–199.
206 A. A. Gokhale, S. Kandoi, J. P. Greeley, M. Mavrikakis and J. A. Dumesic, *Chem. Eng. Sci.*, 2004, **59**, 4679–4691.
207 J. J. Lukkien, J. P. L. Segers, P. A. J. Hilbers, R. J. Gelten and A. P. J. Jansen, *Phys. Rev. E: Stat. Phys., Plasmas, Fluids, Relat. Interdiscip. Top.*, 1998, **58**, 2598.
208 D. Mei, M. Neurock and C. M. Smith, *J. Catal.*, 2009, **268**, 181–195.
209 Y. Choi and P. Liu, *Catal. Today*, 2011, **165**, 64–70.
210 R. Zhu and M. C. Lin, *J. Phys. Chem. C*, 2008, **112**, 14481–14485.
211 D. W. Blaylock, T. Ogura, W. H. Green and G. J. O. Beran, *J. Phys. Chem. C*, 2009, **113**, 4898–4908.
212 http://www2.toyota.co.jp/en/news/10/09/0907.html, TMC, Aisin to Provide Improved Fuel Cells for Test Project.
213 D. Peterson and J. Winnick, *J. Electrochem. Soc.*, 1996, **143**, L55–L56.
214 D. R. Peterson and J. Winnick, *J. Electrochem. Soc.*, 1998, **145**, 1449–1454.
215 M. Liu, P. He, J. L. Luo, A. R. Sanger and K. T. Chuang, *J. Power Sources*, 2001, **94**, 20–25.
216 P. He, M. Liu, J. L. Luo, A. R. Sanger and K. T. Chuang, *J. Electrochem. Soc.*, 2002, **149**, A808–A814.
217 D. Monder, K. Nandakumar and K. T. Chuang, *ECS Trans.*, 2005, **2005–07**, 837–844.